UNIVERSITÀ DEGLI STUDI DI TORINO

Department of Molecular Biotechnology and

Health Sciences

Ph.D. program in

"Molecular medicine"

XXXIV cycle

Dysregulation of FLVCR1-dependent mitochondrial calcium handling in neural stem cells causes congenital hydrocephalus

Francesca Bertino

Tutor: Prof. Deborah Chiabrando

Coordinator: Prof. Emanuela Tolosano

Academic Years: 2018-2023

Table of contents

Abstract

Congenital hydrocephalus (CH), occurring in approximately 1/1000 live births, represents an important clinical challenge due to the limited knowledge of underlying molecular mechanisms. The discovery of novel CH-genes is thus essential to shed light on the intricate processes responsible for ventricular dilatation in CH. Here we identify *FLVCR1* as a novel gene responsible for a severe form of CH in humans and mice. Mechanistically, our data reveal that the heme exporter FLVCR1a interacts with IP3R3-VDAC, a complex located on mitochondrial-associated membranes (MAMs) that controls mitochondrial calcium handling. Loss of *Flvcr1* in mouse neural stem/progenitor cells (NSCs) affects mitochondrial calcium levels and energy metabolism, leading to defective cortical neurogenesis and brain ventricle enlargement. Our findings converge on defective NSCs calcium handling and, consequently, mitochondrial metabolism as a novel pathogenetic mechanism driving CH.

Graphical abstract

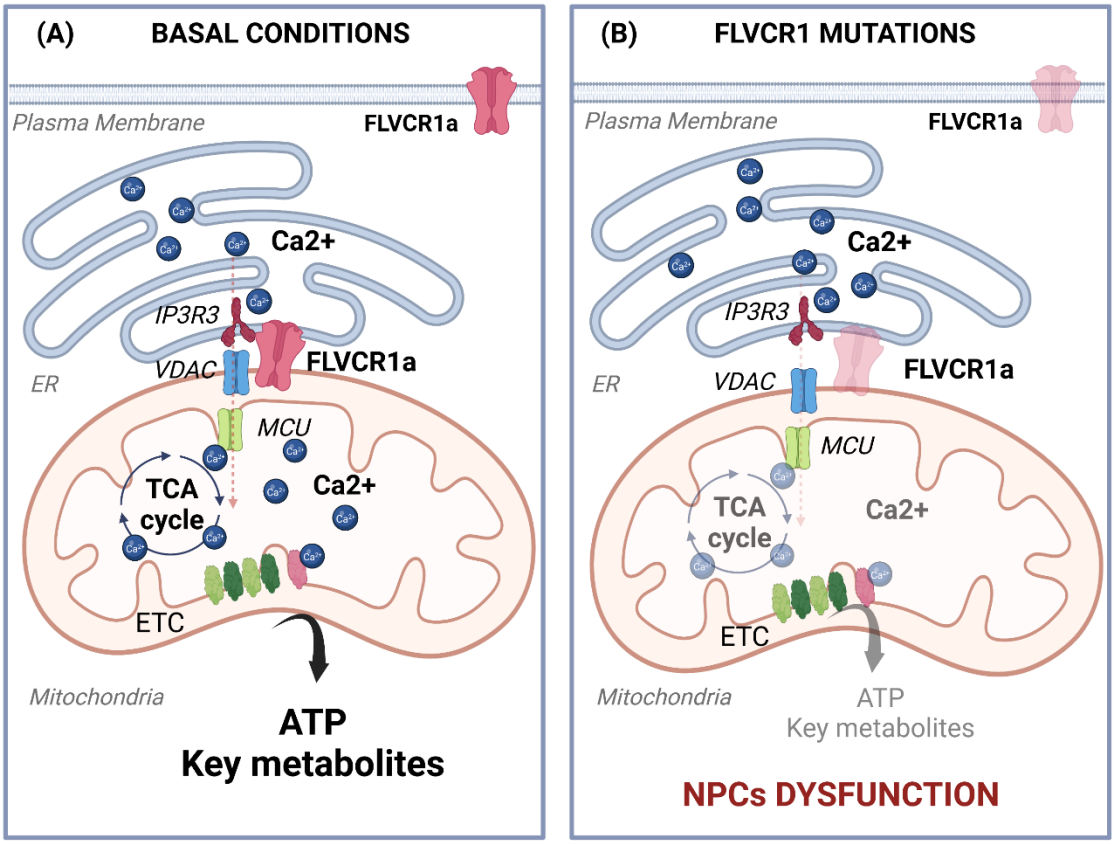

Introduction

Hydrocephalus (gr. “water in the brain”) is a neurological disorder characterized by an enlargement of the cerebral ventricles due to an accumulation of cerebrospinal fluid (CSF). It is one of the oldest known neurological conditions in humans, with evidence of its recognition dating back to ancient Egypt (*1*). Although hydrocephalus can occur at any age, it most commonly affects children and the elderly. In newborns and infants, hydrocephalus can be caused by secondary causes such as hemorrhage or infection (acquired hydrocephalus) or can be classified as primary or congenital hydrocephalus (CH) in the absence of a known antecedent (*2*). CH is a common condition that affects around 1 in 1000 live births and remains the leading reason for brain surgery in children. Common features are an enlarged head, seizures, and developmental delays (*3*).

Ventriculomegaly in hydrocephalus has been largely attributed to overaccumulation of the cerebrospinal fluid (CSF) (*4*). CSF is an ultrafiltrate of plasma contained within the ventricles of the brain and the subarachnoid spaces of the cranium and spine which is produced primarily by the choroid plexus and plays vital roles in nourishing and protecting the brain (*5*),(*6*). However, its overproduction or improper drainage can lead to hydrocephalus. In this “*traditional*” model, CSF accumulation expands the ventricles increasing intracranial pressure (ICP), which compresses the overlying brain tissue, presumably leading to brain damage responsible for poor neurodevelopmental outcomes and, if untreated, lethal brain herniation. However, CH can occur without obvious obstruction of CSF flow, a condition known as communicating hydrocephalus (*7*).

The current treatments aim to reduce CSF volume by neurosurgical CSF diversion (shunting and endoscopy) to reduce ICP and therefore brain damage (*8, 9*). Although these treatments can be lifesaving for many patients, some types of hydrocephalus, including communicating hydrocephalus, may not respond to them. In these cases, intracranial pressure can be paradoxically normal or even low (*10*), and even after successful CSF diversion, ventriculomegaly may persist and neurodevelopmental outcomes can remain poor (*11*). Moreover, CH often presents with a constellation of other structural brain defects not explicable by altered fluid circulation, including open lip schizencephaly, colpocephaly, and polymicrogyria (*12*). All these observations suggest that hydrocephalus may not be caused solely by an excess of CSF in the brain.

Recent groundbreaking genetic studies have revealed that in some cases hydrocephalus may arise from dysregulation of neural stem cells (NSCs) fate during brain development. Whole-exome sequencing (WES) of 381 patients with neurosurgically treated CH has identified

mutations in genes that are key regulators of prenatal neurogenesis (damaging mutations with large effect contributed to 22% of analyzed CH). Therefore, in some instances, hydrocephalus arises from NSCs dysregulation and aberrant neurodevelopment rather than from impaired "*brain plumbing*" (*12, 13*). In this new scenario, named the "*neuroprogenitor-based theory*", the poor cell mass of the neocortex cannot contain the continued CSF production from the unaffected choroid plexus, finally resulting in ventricular enlargement. Despite the great impact that these findings have on CH patients, the molecular pathways implicated in *neuroprogenitor-based CH* cases are still poorly understood and characterization of the mechanisms regulating NSCs function becomes critical to better understand the disease.

Proliferative neural stem cells (NSCs) line the embryonic brain ventricles and own the ability to give rise to all types of neural cells, including all the different neurons that populate the six layers human cortex (*14*). Cortical neurogenesis starts as the neuroepithelial cells amplify by symmetric divisions and give rise to apical radial glial cells (aRGCs), which divide at the ventricular border and constitute the ventricular zone (VZ). aRGCs long processes are used as scaffolds for neuronal migration. aRGCs proliferate by asymmetric divisions, giving rise to basal progenitors, including intermediate progenitor cells (IPCs) and basal RGCs (bRGCs) that populate the subventricular zone (SVZ). Basal progenitors then divide to generate all different subtypes of mature neurons that form the complex six layers structure of the human cortex (*14, 15*).

It is well known that NSCs' function is regulated through a dynamic balance between intracellular and extracellular cues, in particular transcription factors and morphogen signals (*16*). However, recent evidence has uncovered the key influence of a mechanism once considered to be merely permissive: cell metabolism (*17*). Neurogenesis is indeed driven by dynamic metabolic changes. NSCs proliferation is sustained by two metabolic pathways: glycolysis ending in lactate and glutaminolysis (*18-22*). Moreover, a shift from glycolysis to oxidative phosphorylation (OXPHOS) is essential to proceed toward neural differentiation (*23*). Loss of this metabolic balance has been associated with reduced proliferation of NSCs, altered proliferation versus differentiation process, and finally to neurodevelopmental disorders in humans (*21, 24*). However, the contribution of metabolic alterations to the pathogenesis of *neuroprogenitor-based CH* is still completely unexplored.

Here, by analyzing a rare genetic variant in the *FLVCR1* gene associated with CH, we unexpectedly uncovered new mechanistic insights into brain development and CH pathogenesis.

FLVCR1a (Feline Leukemia Virus Subgroup C Receptor 1a), initially identified as an essential heme exporter (*25-27*), is emerging as an important regulator of energetic metabolism (*28*).

FLVCR1a expression is required for the proliferation and survival of a variety of different cell types (*25, 29-32*). During mouse development, FLVCR1a is highly expressed in the nervous system (*26*) and studies in zebrafish showed that FLVCR1a downmodulation leads to hydrocephalus (*33*). However, the role of FLVCR1a in NSCs function has never been explored in detail. In this work, we report the first patient with severe congenital hydrocephalus carrying a homozygous inactivating mutation in the *FLVCR1* gene. Our complementary analyses in human brain specimens, as well as a mouse model of CH that we generated, demonstrate a key role of FLVCR1a in the maintenance of NSCs proliferation and survival through the regulation of mitochondria calcium handling and, consequently, cellular energetic metabolism. Our analysis showed a previously neglected localization of FLVCR1a at mitochondria associated membranes (MAMs), where it interacts with the IP3R3-VDAC-GRP75 complex. Loss of Flvcr1a in NSCs results in altered calcium homeostasis and consequently, impaired cellular energetic metabolism.

Our findings converge on the deregulation of calcium handling, which has also been implicated in other neurodevelopmental disorders (*34*), as a novel pathogenic mechanism driving CH. Moreover, our work has broad implications for our understanding of neural stem cell biology in the context of disease and points to calcium and metabolic regulation as potential therapeutic entry points for CH.

Results

Inactivating homozygous *FLVCR1* mutation causes severe congenital hydrocephalus in humans

We identified for the first-time a human fetus with a severe form of CH carrying mutations in the *FLVCR1* (Feline Leukemia Virus Subgroup C Receptor 1) gene. Sonographic examinations of 32 + 4 and 34 + 5 weeks of pregnancy showed extreme microcephaly with anechoic skull and no evidence of cerebral tissue (Fig. 1A and Fig. S1A, B). The falx cerebri, thalami, tentorium and cerebellum were normal. The internal carotid artery was not detectable on either side by color Doppler sonography. These findings led to a prenatal diagnosis of hydranencephaly (Fig. 1B). The pregnancy was terminated in 34 + 5 gestational weeks with a birth weight of 1590g (-2.18z<1Pz), 41cm body length (-2.31z<1Pz) and 27cm head circumference (-3,6<1Pz). Macroscopic evaluation showed an immature male fetus of the 35th gestational week with microcephaly and hydrocephalus with only rudimentary cerebral structures and no indication of visceral anomalies (Fig. S1C).

Trio-whole exome sequencing revealed a novel homozygous frameshift variant c.160delC, p. Arg54GlyfsTer59 in the *FLVCR1* gene (NM_014053.3, NP_054772.1) and confirmed the heterozygous status of the variant for both parents (Fig. 1C). According to ACMG guidelines c.160delC, p. Arg54GlyfsTer59 in the *FLVCR1* gene is a likely pathogenic variant (Class 4; PVS1; PM2) (*35*).

FLVCR1 encodes two different heme transport protein isoforms, FLVCR1a and FLVCR1b (*26, 27*), that regulate intracellular heme homeostasis and energetic metabolism in several cell types (*29, 30, 32, 36-38*). Partially inactivating mutations in the *FLVCR1* gene have been previously identified (*31, 39, 40*)in posterior column ataxia and retinitis pigmentosa (PCARP) and hereditary sensory and autonomic neuropathy (HSAN) patients. The mutation described here represents the first description of a frameshift *FLVCR1* mutation in homozygosity. The c.160delC mutation occurs in the first exon of the *FLVCR1* gene, thus affecting the abundance of the full-length isoform, FLVCR1a. FLVCR1a is a complex glycosylated 12 transmembrane domain protein composed of 555 amino acids (60kDa). The c.160delC mutation occurs very close to the translational start site, upstream the region coding for the first transmembrane domain of the protein (*36*). The mutation is predicted to give rise to a 112 amino acids (12kDa) protein, which is likely non-functional.

Together, these data indicate that deleterious homozygous mutations in *FLVCR1* caused CH in humans, thus expanding the genetic basis of CH pathogenesis.

***FLVCR1a* is highly expressed during brain development in humans and mice.**

As the genetic studies above indicate an essential role for FLVCR1a during brain development, we determined *FLVCR1* expression patterns during central nervous system development. Published atlases (https://www.brainspan.org/rnaseq/search/index.html; single cell atlas) highlight a 2-fold higher expression level of *FLVCR1a* in the first 24 weeks of gestation, compared to later stages of development (Fig. 2A), with particularly strong expression in apical radial glial cell (RGC) progenitors (https://cells.ucsc.edu/?ds=early-brain&gene=FLVCR1). Immunofluorescence analyses confirmed the enrichment of FLVCR1a in RGCs. Staining performed on human brain slices at PWC11 revealed strong FLVCR1a expression in SOX2+/PAX6+ RGCs, and weaker but still positive staining in TBR2+ intermediate progenitors (IPs) (Fig. 2B). These data are further supported by the analysis of independent transcriptomic datasets, which show greater *FLVCR1a* expression at early time points during human development (Fig. S2A). Of note, *FLVCR1a* expression is reduced but not completely lost in the adult human brain (Fig. S2B, C). In the fetal brain, dataset from Fietz et al. (*41*) highlights a peak of *FLVCR1a* expression in the ventricular zone (VZ) and outer subventricular zone (oSVZ) that declines in the cortical plate (CP) (Fig. 2C). Similarly, another dataset from Pollen et al. (*42*) confirmed enriched expression of *FLVCR1a* in RGCs (Fig. 2D). Notably, a similar expression pattern of FLVCR1a was observed in the mouse brain. We first took advantage of a mouse model we generated, in which we fused Flvcr1 gene with the Myc Tag (*43*). Abundance of FLVCR1a was then assessed at different developmental stages and in the adult brain. Similar to human, FLVCR1a abundance is higher during brain development and drops in the adult brain (Fig. 2E). Moreover, to probe the expression of Flvcr1a more precisely in the developing mouse brain, we performed *in utero* pulse-labeling via intraventricular injection of a CFSE ('FlashTag' (FT)) (*44*). This procedure allows fluorescence tagging of mitotic VZ progenitors lining the ventricles and subsequent tracking of time-locked cohorts of their postmitotic progeny, including neurons, throughout corticogenesis and early postnatal development. We performed FT injections at E13.5, isolated labeled cells at 1hr, 10hr, 24hr and 4 days after injection and then performed qPCR to assess the relative expression of *Flvcr1a* over time. This analysis revealed that *Flvcr1a* expression was highest in RGCs (1hr time point) and progressively declines as RGCs differentiate into IPs and neurons (Fig. 2F).

Collectively, these data indicate that *FLVCR1* expression peaks at early stages of neocortical development, with a specific enrichment in RGCs and IPs in both humans and mice.

Loss of *Flvcr1a* in NSCs impairs neurogenesis and causes congenital hydrocephalus in mice.

To investigate the role of FLVCR1a in central nervous system (CNS) development, we generated mice lacking *Flvcr1a* in neural progenitor cells by crossing mice bearing *Flvcr1a* floxed alleles (*Flvcr1a*$^{fl/fl}$) with mice expressing Cre recombinase under the control of rat-Nestin promoter (NesCRE). *Flvcr1a*$^{fl/fl}$;NesCRE+ embryos were found at expected Mendelian ratios until embryonic day E18.5. However, no viable postnatal *Flvcr1a*$^{fl/fl}$;NesCRE+ mice were found in the offspring (Fig. S3A, B), indicating perinatal lethality. *Flvcr1a* deletion was verified by PCR analyses and subsequently confirmed by qRT-PCR (Fig. S3C, D).

To analyze overall brain morphology and gross structural abnormalities resulting from *Flvcr1a* inactivation, we performed X-ray micro-computed tomography (micro-CT) on control and *Flvcr1a*$^{fl/fl}$;NesCRE+ embryos. Micro-CT analysis showed severe neurodevelopmental defects in *Flvcr1a*$^{fl/fl}$;NesCRE+ embryos compared to controls (*Flvcr1a* $^{fl/fl}$). E18.5 *Flvcr1a*$^{fl/fl}$;NesCRE+ embryos displayed microcephaly, enlarged ventricles, and increased subarachnoid and perivascular spaces (Fig. 3A), closely recapitulating the major clinical findings observed in the human fetus with homozygous *FLVCR1* mutations, and representing a suitable animal model for the study of the human syndrome.

Transcriptomic analysis of E14.5 brains showed differential expression of core genes involved in both neuronal differentiation and NPC proliferation (Fig. S4 A-D). Furthermore, we observed reduced expression of several genes related to CH, including *L1cam* and *Gli3* (Fig.S4 B). We also compared the transcriptomic profile of *Flvcr1a*$^{fl/fl}$;NesCRE+ mice to those of two mouse models of congenital hydrocephalus characterized by activation of *Pik3ca* and disruption of *Prdm16* in neural progenitors (*45, 46*), respectively. This analysis revealed a core set of ~50 genes differentially expressed in the three models with distinct degrees of correlation. Our model appeared closer to Pik3ca-overexpressing embryos than to Prdm16-deleted animals, hinting at the impairment of some metabolic pathway in our model. (Fig. S4E).

These data suggest that defective neurogenesis contributes to CH in the absence of *Flvcr1a*. To analyze the impact of *Flvcr1a* loss on neurogenesis, we performed immunofluorescence staining of coronal brain sections. We observed reduced numbers of PAX6+ neural progenitors as early as E14.5, and an associated small but significant increase in the proportional thickness of the TUJ1+ neuronal layer in the developing cortex of *Flvcr1a*$^{fl/fl}$;NesCRE+ embryos compared to heterozygous mutants (Fig. 3B). *Flvcr1a*$^{fl/fl}$;NesCRE+ embryos also displayed reduced numbers of TBR2+ IPs (Fig. 3C). Similarly, cells expressing the layer specific markers TBR1 and CTIP2 are less

abundant (Fig. 3D, E). Noteworthy, the same alterations persist in *Flvcr1a*$^{fl/fl}$;NesCRE+ embryos at subsequent developmental stages (E16.5) (Fig. S5).

To evaluate whether alterations in cell proliferation or, alternatively, in cell death, account for the reduced cell number at E14.5, we performed *in vivo* EdU labeling and TUNEL assay, respectively. EdU was injected into pregnant dams 2 hours prior to sacrifice and embryos were collected at two different developmental stages (E14.5 and E16.5). We found a significant reduction in the number of total EdU+ proliferative cells at E14.5 and E16.5, as well as a reduction in the number of both EdU+/PAX6+ and EdU+/TBR2+ cells (Fig. 4A-F). TUNEL analysis also revealed increased apoptosis in the cortex of E14.5 *Flvcr1a*$^{fl/fl}$;NesCRE+ embryos compared to *Flvcr1a* $^{fl/+}$; NesCRE+ mice (Fig. 4G). Taken together, these data indicate that *Flvcr1a* loss results in reduced RGC and IP proliferation, precocious neuronal differentiation of IPs and mature neurons, and enhanced cell death, suggesting that FLVCR1a is essential for NPC proliferation, differentiation, and survival.

FLVCR1a interacts with IP3R3-VDAC complex at MAMs.

To elucidate how FLVCR1a may regulate neural progenitor function, we investigated the FLVCR1a interactome using the Tandem Affinity Purification (TAP) strategy coupled to tandem mass spectrometry. The FLVCR1a protein complex was first purified from HEK293 T-Rex Flp-in cells overexpressing FLVCR1a fused with a small tag (TAP Tag), which does not affect protein expression and localization (Fig. S6B). The FLVCR1a protein complex was subsequently isolated (Fig. S6C), analyzed on a SDS gel and subjected to mass spectrometry. To discriminate false positive interactors, the empty vector expressing the TAP-tag alone was used as negative control. The top 50 FLVCR1a interactors are shown (Fig. S6C), stratified based on the ratio of FLVCR1a-TAP pulldown/empty and sorted top to bottom from highest to least enriched proteins. The extensive analysis of the interactome showed an enrichment of components of mitochondria, of ER and of mitochondria associated membranes (MAMs) (Fig. 5A, B and Fig. S6D). As FLVCR1a has been described as a plasma membrane heme exporter (*26*), these data suggest an alternative localization of the protein. Immunofluorescence analysis showed the endogenous FLVCR1a protein localizes both at the plasma membrane and intracellularly (Fig. 5C). To determine the subcellular localization of FLVCR1a, we performed subcellular

fractionation to discriminate ER, MAMs, and pure mitochondria. This analysis showed that FLVCR1a protein is enriched in the MAMs fraction, highlighting a previously unknown localization of FLVCR1a transporter at MAMs (Fig. 5D and Fig. S6E). Interestingly, among all the identified FLVCR1a interactors we found the IP3R3, VDAC and GRP75 proteins, which form a complex at mitochondria associated membranes (MAMs) mediating calcium transfer from the endoplasmic reticulum (ER) to mitochondria (*47*). Mitochondrial calcium is a positive regulator of various aspects of mitochondrial metabolism, which has recently been implicated in the regulation of NPC proliferation (*17, 21-23, 48*). To confirm the interaction between FLVCR1a and the IP3R3-VDAC1-GRP75 complex, we purified FLVCR1a-TAP and performed western blot analysis for endogenous IP3R3 and VDAC (Fig. 5E) and found that both proteins co-immunoprecipitated with FLVCR1a. Moreover, immunofluorescence analysis of endogenous FLVCR1a revealed that FLVCR1a partially localizes intracellularly and FLVCR1a localizes in close proximity to IP3R3, VDAC and GRP75 (Fig. 5F). Using Proximity Ligation Assay (PLA), we confirmed the endogenous interaction between FLVCR1a and VDAC, FLVCR1a and IP3R3, as well as between FLVCR1a and GRP75. Antibodies for proteins not interacting with FLVCR1a have been used in pairs with FLVCR1a as negative controls. PLA indicates a tight endogenous interaction between FLVCR1a and IP3R3, VDAC and GRP75, as demonstrated by signal quantifications (Fig. 5H). Finally, immunoprecipitation of endogenous FLVCR1a followed by immunoblotting for VDAC confirmed an interaction between endogenous FLVCR1a and VDAC (Fig. 5G). Taken together, these data demonstrate that FLVCR1a also localizes at MAMs, where it interacts primarily with VDAC and with IP3R3 and GRP75.

FLVCR1a regulates ER-mitochondria membrane tethering and mitochondrial calcium uptake.

As the IP3R3-VDAC complex localizes at MAMs and regulates ER-mitochondria membrane tethering, we investigated whether *FLVCR1a* loss in human cells results in MAMs impairment. To this end, we analyzed the number of ER-mitochondria contact sites in HeLa cells upon *FLVCR1a* downregulation (Fig. 6A) by confocal microscopy, using the two fluorescent proteins sec61-GFP and mt-DsRed to visualize the ER and mitochondria, respectively. Colocalization of the two fluorophores was then quantified as a proxy for ER-mitochondria membrane contacts. Interestingly, we observed a significant reduction in the number of MAMs upon *FLVCR1a* silencing, as quantified by Mander's colocalization coefficients and by Pearson correlation coefficient (Fig. 6B). Moreover, a decrease in ER-mitochondria tethering was further confirmed

by PLA using the IP3R3-VDAC antibody pair (Fig. 6C, D). To exclude the possibility that decreased abundance of IP3R3 and VDAC contribute to the observed reduction in MAMs, we analyzed their expression in *FLVCR1a*-silenced HeLa cells, but no alterations were observed (Fig. 6E), confirming that *FLVCR1a* downmodulation disrupts MAMs in HeLa cells.

As the IP3R3-VDAC complex mediates calcium influx from the endoplasmic reticulum to mitochondria, we next investigated whether the modulation of FLVCR1a affects the activity of the complex. We analyzed HeLa cells expressing mtAEQmut, an aequorin-based calcium probe located in the mitochondrial matrix. The administration of histamine acts on Gq-coupled plasma membrane receptors and causes the production of inositol 1,4,5 trisphosphate (IP3), thus inducing the release of calcium from the ER to mitochondria and its consequent, transient, accumulation within mitochondrial matrix (*49*). The efficiency of the ion transfer between the two compartments is highly sensitive to the status of MAMs (*50*). The elevation of mitochondrial calcium concentration was significantly limited in *FLVCR1a*-deficient *vs* proficient HeLa cells (Fig. 6F, G), and reduced calcium influx in mitochondria was further confirmed using the FRET-based mitochondrial calcium reporter, 4mtD3CPV (Fig. S7A). Importantly, cytosolic calcium was almost unaffected upon *FLVCR1a* silencing (Fig. S7B), supporting the idea that *FLVCR1a* downregulation specifically impairs ER to mitochondria calcium transfer through the IP3R3-VDAC1 complex and unveiling an important functional role of FLVCR1a at MAMs.

To better dissect the role of FLVCR1a in MAMs regulation, we analyzed HeLa cells overexpressing a Myc-tagged FLVCR1a protein (Fig.6H). Interestingly, overexpression of FLVCR1a resulted in increased ER-mitochondria contact sites, as demonstrated by colocalization analysis of the two intracellular organelles (Fig. 6I). Finally, increased mitochondrial calcium uptake was observed in HeLa cells overexpressing FLVCR1a protein upon histamine stimulation (Fig. 6J, K). These additional data further support the role of FLVCR1a in the maintenance of MAMs integrity and regulation of mitochondrial calcium uptake.

As mutations in *FLVCR1a* have been described in patients with PCARP/HSAN (*31, 39, 40, 51*), we sought to investigate if altered MAMs and mitochondrial calcium homeostasis can be observed in human primary fibroblasts carrying *FLVCR1* mutations. To achieve this, we analyzed FLVCR1a abundance, the extent of MAMs, and ER to mitochondria calcium fluxes in patient cells compared to cells from control subjects. Interestingly, FLVCR1a is still expressed in patient-derived cells, but at lower levels (Fig. 7A). Moreover, we observed a decrease in the extent of MAMs in these cells, as demonstrated by PLA analysis using the IP3R3-VDAC antibody pair (Fig. 7B). IP3R3 and VDAC abundance was unchanged, suggesting that the reduced number of PLA

positive dots is due to the decreased number of ER-mitochondria contact sites rather than to a decreased content of these proteins (Fig. 7C, D). Of note, we observed a dramatic defect in mitochondrial calcium uptake in patient-derived cells as compared to control subjects (Fig. 7E, F). Mitochondrial calcium homeostasis is essential for the proper maintenance of mitochondrial energetic metabolism, being calcium an essential cofactor of several TCA cycle dehydrogenases, as well as of some electron transport chain (ETC) complexes, ATP synthase included (*52*). Therefore, reduced concentration of mitochondrial calcium contributes to impaired oxidative metabolism and ATP production. Interestingly, patient-derived fibroblasts showed reduced mitochondrial ATP concentrations compared to controls (Fig. 7G). However, ATP content is almost completely rescued upon over-expression of the mitochondrial calcium uniporter (MCU). Similarly, the activity of ETC I–II-III and IV is reduced in patients' cells but restored upon MCU overexpression (Fig. 7H-K), supporting the notion that altered mitochondrial calcium levels account at least in part to the metabolic defect observed in patient fibroblasts.

Overall, the findings support a previously undescribed role of FLVCR1a in the regulation of ER-mitochondria membrane tethering and mitochondrial calcium transfer through its interaction with the IP3R3-VDAC1 complex at MAMs.

Loss of *Flvcr1a* in NSCs impairs mitochondrial calcium handling and energetic metabolism.

Proper mitochondrial calcium handling and regulation of energetic metabolism are essential for the proliferation of NSCs (*34, 53*). Interestingly, RNAseq analysis underscores deregulation of calcium and mitochondrial energetic metabolism in whole brains from *Flvcr1a*$^{fl/fl}$;NesCRE+ embryos (Fig. 8A, B). In agreement with these data, we observed a reduction in the activity of ETC complexes, of adenine nucleotide translocase (ANTs), and in the amount of mitochondrial ATP in whole brain from *Flvcr1a*$^{fl/fl}$;NesCRE+ mutants (Fig. S8). To investigate whether impaired MAMs structure and function contribute to defective CNS development in *Flvcr1a*$^{fl/fl}$;NesCRE+ embryos, NSCs were isolated from E12.5 *Flvcr1a*$^{fl/fl}$;NesCRE+ and *Flvcr1a* $^{fl/+}$;NesCRE+ embryos. Mitochondrial calcium influx was measured upon stimulation with the cholinergic agonist carbachol, which activates Phospholipase C (PLC) to promote phosphoinositide hydrolysis and the production of IP3. We found that calcium influx from ER to mitochondria is severely impaired in *Flvcr1a*$^{fl/fl}$;NesCRE+ NSCs (Fig. 8C). These data highlight the important role of FLVCR1a in the maintenance of MAMs integrity and mitochondrial calcium homeostasis in NSCs.

Considering that mitochondrial calcium regulates TCA cycle flux and OXPHOS (*17, 53*), we next examined cellular energetic metabolism in NSCs from *Flvcr1a* mutant mice. The analyses showed

an overall reduction in energetic metabolism in *Flvcr1a*$^{fl/fl}$; NesCRE+ derived NSCs when compared to heterozygotes, as indicated by the reduced activity of calcium-dependent TCA cycle dehydrogenases (pyruvate dehydrogenase, isocitrate dehydrogenase and αketoglutarate dehydrogenase) (Fig. 8D). Likewise, the activity of electron transport chain complexes was reduced (Fig. 8E), as well as the final amount of mitochondrial ATP (Fig. 8F).

Collectively, the data demonstrate that *Flvcr1a* deficiency in NSCs results in reduced mitochondrial calcium and impaired mitochondrial activity, which likely accounts for decreased NPC proliferation and survival, thereby contributing to defective CNS development.

Mutations in the ER calcium-ATPase SERCA2 in patients with CH

The identification of FLVCR1 as a novel CH-gene implicated in the regulation of calcium handling in NSCs, suggests that dysregulation of calcium homeostasis might represent a previously unrecognized pathogenetic mechanism driving CH. To understand whether dysregulation of calcium homeostasis might have a broader impact on the pathogenesis of CH, we evaluated whether genes-related to calcium homeostasis are mutated in patients with CH. To address this issue, , we analyzed a large patient-parent trio cohort of exome-sequenced physician-diagnosed congenital hydrocephalus patients. We did not find any mutations in FLVCR1, IP3R3, VADC genes. This analysis revealed a damaging de novo missense variant in a highly conserved residue (p.G769R) of the gene ATP2A2 (SERCA2) and this variant has previously been interpreted as pathogenic in ClinVar. SERCA2 is a calcium-ATPase essential for calcium import into the ER (*54*). Our wider genetic analysis expands the spectrum of patients with CH carrying mutations in genes regulating cellular calcium homeostasis and supports calcium dyshomeostasis as a pathogenic mechanism in CH.

Discussion

The analysis of rare genetic variants associated with CH can provide new mechanistic insights into brain development. The data reported herein describe an inactivating homozygous *FLVCR1* mutation in a human fetus with severe CH and identify a previously unknown function for FLVCR1a during CNS development. FLVCR1a is a recognized plasma membrane heme exporter necessary to control intracellular heme levels in multiple cell types (*26, 28-30, 37, 38, 43, 55*). The present work explored for the first time the localization of endogenous FLVCR1a protein, demonstrating that, in addition to the plasma membrane, FLVCR1a also localizes at MAMs. Being FLVCR1a a heme exporter (*26, 56*), our findings raise the intriguing possibility that this protein may also be involved in the delivery of newly synthesized heme from mitochondria (the site of heme synthesis) to the ER (the site of heme incorporation into several hemoproteins). This hypothesis is in line with previous studies suggesting that heme transfer between the two organelles may occur at ER-mitochondria contact sites (*57-59*) and with studies showing reduced activity of ER-resident hemoproteins upon *FLVCR1a* loss (*37*). Mechanistically, we demonstrate that FLVCR1a interacts with the VDAC-IP3R3 complex and regulates its function. We found that modulation of FLVCR1a expression reduced mitochondria-ER contacts sites and mitochondrial calcium influx in HeLa cells, primary human fibroblasts, and NSCs from *Flvcr1a* mutant mice. Both heme and calcium are essential to sustain energetic metabolism: heme is a cofactor of the electron transport chain (ETC) enzymes, regulates the transcription of glycolytic genes and mitochondrial ETC genes, and influences the translocation of ATP across mitochondrial membranes (*28, 60-62*); likewise, mitochondrial calcium influx regulates mitochondrial bioenergetics by controlling the activity of enzymes involved in the TCA cycle and ETC (*52*). Coherently, we found a profound impairment of oxidative metabolism upon *FLVCR1a* loss. Based on these observations, we propose that the interaction between FLVCR1a and the VDAC-IP3R3 complex might be necessary to coordinate heme synthesis with mitochondrial calcium influx to properly regulate mitochondrial bioenergetics, especially during neurogenesis.

Our study converges on the notion that FLVCR1a is necessary for neurogenesis by regulating MAMs structure and function. Indeed, loss of *Flvcr1a* affects mitochondrial calcium handling and energetic metabolism in NSCs and impairs mouse embryo neurogenesis. Noteworthy, other proteins essential for NPC proliferation have been reported to regulate mitochondrial calcium levels. Specifically, the protein product of the microcephaly gene MCPH1 interacts with the IP3R3-VDAC complex to sustain calcium influx in mitochondria. Moreover, ARHGAP11b protein, essential for neocortex expansion in humans, interacts with and inhibits the mitochondrial permeability transition pore (mPTP), blocking calcium release from mitochondria. This cooperation is essential for proper maintenance of NPC metabolism and proliferation (*63*). Our work proposes FLVCR1a as an additional key regulator of NPC function through the modulation

of mitochondria calcium homeostasis and energetic metabolism. FLVCR1a, together with MCPH1 and ARHGAP11B, cooperates to maintain normal calcium homeostasis in mitochondria. When proper calcium homeostasis is lost, mitochondrial metabolism is compromised together with NPC function and neocortex development. On a more general note, our data corroborate the notion that mitochondrial dynamics and metabolism exert key roles in neural stem cell maintenance. Reduced NPC proliferation appeared to be a pivotal driving mechanism of CH upon *Flvcr1a* loss. Indeed, loss of *Flvcr1a* caused premature differentiation of NSCs at the expense of stem and progenitor cells maintenance, leading to overall reduction in cortex thickness. As recently demonstrated, cortical hypoplasia can affect brain biomechanics and its ability to resist mechanical strain, resulting in a secondary expansion of ventricles in the absence of a primary defect in CSF dynamics (*13*). Thus, our results corroborate the neuroprogenitor-based paradigm of CH (*12, 13*).

Altogether, these observations sustain the notion that the alteration of mitochondrial calcium handling and energetic metabolism can lead to both microcephaly and CH. These two apparently opposite disorders are not mutually exclusive. Studies have shown that ventricle enlargement can be a secondary complication of microcephaly (*13*). Furthermore, genetic and computational studies showed a genetic overlap between CH and microcephaly (*12, 13*), thus suggesting the existence of common molecular mechanisms.

Emerging evidence sustains that the alteration of calcium homeostasis might be an important mechanism contributing to different forms of CH. Mutations in *PIK3CA*, *PTEN* and *MTOR* have been recently identified in a subset of patients with sporadic CH (*12*), and studies in animal models support a role for PI3K signaling during neurogenesis. As PI3K participates in the control of calcium handling by regulating the phosphorylation of IP3R3, we can speculate that calcium dysregulation can contribute to the pathogenesis of these specific subtypes of CH. It is also worth noting that the heme importer FLVCR2, responsible for CH in both humans and mice (*64-66*) was recently discovered to interact with the calcium transporter SERCA (*67*). We also described novel pathogenic variants in SERCA2 in patients with CH. Taken together, these observations suggest that alteration of mitochondrial calcium homeostasis may have a broader than expected impact in CH-pathogenesis.

Our study improves the understanding of the molecular pathogenesis of CH, highlighting dysregulated calcium homeostasis as a new pathogenetic mechanism in CH. Furthermore, our results provide important cues for the comprehension of PCARP/HSAN originating from partially inactivating mutations in *FLVCR1*. The alteration of MAMs structure and function observed in

patients' fibroblasts suggest that alteration of calcium handling might contribute to PCARP/HSAN pathogenesis. Supporting this concept, mutations in *IP3R3* have been found in patients with Charcot Marie Tooth disorder (CMT), a motor neuropathy (*68*). Moreover, alterations in proteins regulating organelle-membrane shaping, ER-mitochondria contact sites, and mitochondrial calcium handling have been described as underlying determinants of several sensory neuropathies with pain loss (*69, 70*). As enhancers of calcium uptake in mitochondria already exist and are currently used in clinics to treat several neurological disorders, our work also puts forward the development of new treatments for these rare neurological diseases.

Materials and Methods

Patient/Human fetus

A consanguineous couple from the United Arab Emirates (1st degree and 2nd degree cousins; see Pedigree Fig.1) presented for evaluation of extreme fetal microcephaly. The pregnancy occurred after *in vitro* fertilization and preimplantation diagnosis with numerous chromosomal disorders. The pregnancy was terminated in 34 + 5 gestational weeks with a birth weight of 1590g (-2.18z<1P), 41cm body length (-2.31z<1P) and 27cm head circumference (-3,6<1P).

Written informed consent was given for investigation and publication according to the German Genetic Diagnostics Law.

Whole Exome Sequencing

For Variant analysis and interpretation, the following softwares were used: SeqNext 4.0 (JSI Medicals), Variant Studio 3.0 (Illumina) and the Moon Software 4.0.1 (Diploid/Invitae). DNA was extracted from amniotic fluid and parental blood samples for Trio Whole Exome Sequencing (Trio-WES). Investigation of the coding areas including adjacent intron regions of the Trio-whole exome was performed using high-throughput sequencing from genomic DNA (xGen Exome Research Panel v2; 19,433 genes; Integrated DNA Technology). The genomic DNA was processed using the hybrid capture method, relevant areas were enriched and amplified by PCR (Lotus DNA Library Prep Kit, IDT) and sequenced by massive parallel sequencing on the NextSeq 550 system (Illumina). Our quality criteria require a minimum coverage of 20 sequences per base for at least 96% of the target areas of all genes examined. For Variant analysis and interpretation, the following Softwares were used: SeqNext 4.0 (JSI Medicals), Variant Studio 3.0 (Illumina) and the Moon Software 4.0.1 (Diploid/Invitae). The analysis revealed a frameshift variant c.160delC, p. Arg54GlyfsTer59 in the FLVCR1 gene in the homozygous state in the fetus and in the heterozygous state in each parent. These results were confirmed by conventional Sanger sequencing.

Mouse Lines

Flvcr1a$^{fl/fl}$ mice have been described previously (*37*). To generate *Flvcr1a*$^{fl/fl}$; Nes-cre mice, *Flvcr1a*$^{fl/fl}$ mice were crossed to mice expressing Cre recombinase under control of nestin promoter (Nes-Cre). Nes-Cre mice were purchased from the Jackson Laboratory (B6. Cg-Tg(Nes-cre)1Kln/J Strain #:003771). Experiments on mice followed European legislation (Directive 2010/63/EU), concerning housing, husbandry, and animal welfare. The experimental procedures were approved by the Italian Ministry of Health (Approval number n° 604/2021-PR)

The FLVCR1-myc line was generated by CRISPR/Cas9, inserting the GAA CAA AAA CTC ATC TCA GAA GAG GAT CTG MYC sequence in frame at the 3' end of the FLVCR1 coding region. For this, a sgRNA targeting the sequence AAT CTT CAC TCT GAA GAA GC was generated by in vitro transcription. Briefly, oligonucleotides AGG GAA TCT TCA CTCT GAA GAA GC and AAA CGC TTC TTC AGA GTG AAG

ATT were annealed and cloned into the BssI sites of plasmid pgRNA-basic. The sgRNA was transcribed from the resulting plasmid with the MEGAshortscript T7 Kit (Life Technologies) and purified with the MEGAclear Kit (Life Technologies). Cas9 mRNA was produced by *in vitro* transcription from the pT7-Cas9 plasmid using the mMESSAGE mMACHINE T7 Ultra Kit (Life Technologies) and purified with the MEGAclear Kit. The purified gRNA was microinjected into fertilized FVB/N mouse oocytes together with the Cas9 mRNA and the synthetic ssDNA 5'-AGT TGA TAG TCG GGT AGA TCC AAA ACC CAA AGT GAT GGT GTC TAT ACA GTC GGA ATC TTC ACT CGA ACA

AAA ACT CAT CTC AGA AGA GGA TCT GTG AAG CCG GTG TGG CTG CCC CTC AAC ATG GGC ATG TGG CTT CGT CTT TGG GCA GCT GTG TGA GGTG-3'. The edited alleles were confirmed by direct sequencing of the target region. Genotyping of embryos was performed by PCR. The primers used for genotyping are listed below. Mice used at Instituto Gulbenkian de Ciência (IGC) were bred and

maintained under specific pathogen-free (SPF) conditions. Protocols were approved in a two-step procedure, by the Animal Welfare Body of the IGC and by the Portuguese National Entity that regulates the use of laboratory animals in research (DGAV—Direção Geral de Alimentação e Veterinária). Experiments on mice followed the Portuguese (Decreto-Lei nº 113/2013) and European (Directive 2010/63/ EU) legislation, concerning housing, husbandry, and animal welfare. C57BL/6J wild-type mice were obtained directly from the IGC animal facility.

PCR

Mice and embryos genotyping was performed using the following primers:

Sequenze primers	
Cre Fw	GGACATGTTCAGGGATCGCCAGGCG
Cre Rev	GCATAACCAGTGAAACAGCATTGCT
FLVCR ILox Fw	TCTAAGGCCCAGTAGGACCC
FLVCR ILox Rev	GAAAGCATTTCCGTCCGCCC

FLV-COND Fw (cioe` FLVCR-IILox Fw)	GGCCTCAACTGCCTGGGAGC
FLV-COND Rev (cioe` FLVCR-IILox Rev)	AGAGGGCAACCTCGGTGTCC

PCR CRE:

Cre Fw

Cre Rev

PCR I Lox:

I Lox Fw + I Lox Rev

PCR Delezione (a 3 primers):

I Lox Fw + II Lox Fw + II Lox Rev

PCR Delezione (a 2 primers):

II Lox Rev (o FLVC COND Rev) + I Lox Fw

PCR MYC:

Flvcr1-chkF1 GCTGCATCTCCTGAGTGTCAG

Flvcr1-chkR1 AGCACAATCGCTGATTAACAC

Flvcr1-chkF2 CTCATCTCAGAAGAGGATCTG

Flvcr1-chkR2 CAGATCCTCTTCTGAGATGAG

"Flashtag" in utero injections

"Flashtag" labeling of enriched cell populations in wild type mice was conducted for a separate pilot experiment in the Panagiotakos lab, as described below. A portion of the RNA collected for that experiment was used for this study. This experiment was conducted under animal protocols approved by the UCSF Institutional Animal Care and Use Committee and in accordance with National Institutes of Health guidelines for the care and use of laboratory animals. Prior to surgery, "Flashtag" working solution was prepared according to Govindan et al., 2018. Specifically, 8µl of DMSO and 1µl of 0.01% Fast Green was added to one vial of CellTrace CFSE

(Thermo Fisher, C34554). Glass micropipettes were pulled and beveled to produce a fine pointed tip 30-70µM in outer diameter.

For “Flashtag” injections, E13.5 timed-pregnant Swiss Webster dams (E14, Charles River Labs) were anesthetized with isofluorane (2-4% to effect). Multimodal analgesia (0.1mg/kg Buprenorphine hydrochloride and 5mg/kg Carprofen) was administered preoperatively via subcutaneous injection. Aseptic technique was used throughout the procedure. The uterine horns were exposed via a midline incision and gently lifted out of the abdominal cavity onto sterile gauze pads. The abdominal cavity was continuously bathed in pre-warmed, sterile saline throughout the surgery. 0.5µl of “Flashtag'' was injected into the lateral ventricle of individual embryos using a beveled micropipette. After all embryos were injected, the uterine horns were gently returned to the abdominal cavity, bathed one final time in warm saline, and the incision was closed in two layers. Lidocaine was applied locally prior to incision closure. Animals recovered in heated recovery cages and were returned to their home cages once they were alert and ambulating normally(*44*).

FACS

1hr, 10hrs, 24hrs, and 4 days after Flashtag injection (corresponding to the labeling of radial glia, intermediate progenitor cells, newborn neurons and postmitotic neurons, respectively), pregnant dams were sacrificed, and embryonic brains were dissected in ice cold HBSS. For the 1hr and 10hr post-injection time points, the ventricles of dissected brains were flushed with a pipette to dilute any residual “Flashtag” solution. The meninges were carefully removed from the brains, and individual cortical hemispheres were dissected and processed separately in downstream steps. Cortices were digested with papain (Worthington, LS003119) for 7 min at 37C and subsequently bathed in Trypsin Inhibitor (Sigma Aldrich, SIAL-T9253-1G) and dissociated into single cell suspensions in ice cold HBSS with DNAse. Cortical hemispheres were then separately sorted on a BD FACS Aria. Dead cells were excluded using Sytox Red (Life Technologies, S34859), and the top 5-10% of “Flashtag''-expressing cells were collected in Buffer RLT (from the Qiagen RNeasy Micro Kit, 74004). Parameters for FACS gates were set up as described in (*44*).

qRT-PCR

RNA was extracted using the Qiagen RNeasy Micro kit. RNA quality and concentration was confirmed using the Agilent BioAnalyzer, and cDNA was made using the Superscript III kit (Invitrogen, 11752050). qPCR was then performed using the LightCycler® 480 SYBR Green I Master (Roche) with primers designed to specifically target each gene of interest. Technical

duplicates or triplicates were performed, and Ct values were normalized to Actb levels. Replicates were discarded if Ct values varied greater than 0.5 Ct values. A transcript's relative abundance was calculated as follows: (Etarget–Ct (target)) / (EActB–Ct (ActB)). Primers used are listed below:

mouse-Actb-forward: TGA CGT TGA CAT CCG TAA AG

mouse-Actb-reverse: GAG GAG CAA TGA TCT TGA TCT

mouse-Flvcr1a-forward: CCGTCGCCTCGGTATGG

mouse Flvcr1a-reverse: CACTAAAACAGGTGGCAACAAAAA

Micro-CT

Micro computed tomography (Micro-CT) analysis was performed on 18.5d mouse embryos using a Bruker Skyscan 1172 micro-CT. Embryos were fixed in formalin and then stained for 15 days with a soft tissue contrast agent (phosphotungstic acid (PTA) 2.5% dissolved in water). Acquisitions were performed at 80KV using a 0.5mm Al filter at a resolution of 7 µm, 0.6° of rotation step, 360° scan, 4x frame averaging.

Cell lines

HEK293 and Flp-In T-Rex 293 cells were cultured in Dulbecco's modified Eagle's medium (DMEM; Gibco) supplemented with 10% fetal bovine serum (Gibco). Human fibroblasts were cultured in DMEM, supplemented with 10% fetal bovine serum and 1% Non-Essential Amino Acid (NEAA) (Gibco).

Cell transient transfections and plasmids

Transient transfection in Hek293T cells was performed using LIPOFECTAMINE 2000 (Thermofisher, Ref 11668019) following manufacturer instructions. Transient transfections in NSCs were performed using jetOPTIMUS DNA transfection Reagent (Polyplus, Ref 101000025). NSCs were seeded and cells analyzed 24 hours after transfection.

Experiments were performed using the following plasmids: pCMV-mito-GEM-GECO1 (Addgene plasmid #32461), FLVCR1a-myc cDNA was cloned in plvx-puro vector (Addgene) as previously described (*40*). pAc-GFPC1-Sec61beta (Addgene plasmid #15108), DsRed was cloned into pcDNA3, in frame with the mitochondria localization sequence of human COX8 as previously described (*71*), mitochondrial aequorin was cloned into pcDNA3 as described in (*72*).

Immunostaining

Cells grown on glass coverslips were fixed with 4% paraformaldehyde (PFA) in phosphate buffered saline for 10 minutes at room temperature, and then permeabilized with 0.1% Triton X- 100 in PBS for 10 minutes. Cells were subsequently incubated with FLVCR1 primary antibody (Santa Cruz Biotechnology, Dallas, TX USA, catalog n° sc-390100; 1:50) and VDAC1 antibody (Abcam ab154856, 1:100) for 60 minutes at room temperature. Dapi was used to label the nucleus (Sigma Aldrich diluted 1:500; Sigma Aldrich). Alexa-488 or Alexa-594 secondary antibodies (diluted 1:1000; Thermo Fisher Scientific) were incubated with the cells for 60 minutes at room temperature. Confocal image acquisition was performed with a Leica TCS SP8 confocal system (Leica Microsystems) with a HC PL APO 63 ×/1.30 OIL CS2 objectives.

Human tissues and Immunostaining

Human tissues were obtained from the Gynecology-Obstetric Department at Robert Debre Hospital, Paris, according to the rules established by the French Bioethics Agency and with parental consent. 8- 10 or 13 Post Conception Weeks (PCW) fetal brains were obtained after volunteer abortion or spontaneous pregnancy termination, respectively. After 24 hours fixation in 4% PFA, tissues were cryoprotected in 15% sucrose in PBS, frozen in isopentane at -50°C, and kept at -80°C. Transverse 20 micron-thick sections were cut on a Leica CM 3050 cryostat and kept à -80°C until use. Antigen retrieval was performed by heating sections in 50 mM citrate buffer pH 6 for 20 minutes at 95°C. After rinsing in PBS, sections were incubated overnight at 4°C with primary antibodies diluted in Bond Primary Antibody Diluent (LEICA; Ref AR9352). The antibodies were mouse anti FLVCR1 (Santa Cruz Biotechnology; sc-390100; 1:500) and rabbit anti PAX6 (Proteintech; ref 12323-1-1P; 1/2000), anti SOX2 (Abcam; ref ab97959; 1/2000) and anti TBR2 (Abcam; ab23345; 1:250). After two 10 minutes washes in PBS, sections were incubated in highly absorbed goat anti-mouse and goat anti rabbit IgG, coupled to either Alexa-480 (Invitrogen) or Cy3 (Jackson) diluted 1:2000, for 2 hours at room temperature. 1 □g/ml DAPI (4',6-diamidino-2-phénylindole; SIGMA) was added to the secondary antibody solution. After rinsing in PBS, sections were mounted in Fluoromount-G (SouthernBiotech).

Imaging of human tissues

Imaging was performed using a Leica TCS SP8 confocal scanning system (Leica Microsystems) equipped with 405-nm Diode, 488-nm Ar and 561-nm DPSS lasers. A 20x HC PL APO oil-immersion objective was used to take tiles images in a sequential mode and with a 1024x1024 resolution. Pictures with composite colors and the corresponding Tiff files were generated on

ImageJ and further processed on Photoshop C6 for sizing and eventually for improving color contrast.

RNA Sequencing

Total RNA from whole E14.5 embryo brain was isolated with RNAeasy Plus Micro kit (Qiagen). Sequencing libraries were constructed from total RNA with RIN>7 using the NEBNext Ultra II RNA Library Prep Kit (New England Biolabs, MA). Unstranded libraries were sequenced using a HiSeq4000 system (Illumina, CA) to produce ~40 million 150 pb paired-end reads. After demultiplexing, fastq files were aligned to the mouse genome (mm10) with Rsubread 2.10 and quantified using FeatureCounts. Differential expression analysis was performed with DESeq2 1.36. Volcano plots were rendered using the EnhancedVolcano 1.14 package and heatmaps were made with the pheatmap 1.0 package. Overrepresentation analysis was performed using PANTHER 17.0.

FLVCR1 scRNA-seq Differential Expression Analysis

Differential expression of FLVCR1 was determined in a previously described scRNA-seq atlas of the human brain spanning the period between early-fetal development into adulthood (*73*). The FindAllMarkers (data set, features = 'FLVCR1', logfc.threshold = 0, min.cells.feature = 0, return.thresh = 1) function from the Seurat package in R ((*74*); version 3.2.0) was used to calculate the natural log fold change of the average expression of FLVCR1 between each cluster of interest and all other clusters in the data set. Differential expression was based on a non-parametric, two-sided Wilcoxon rank sum test with p-values adjusted through Bonferroni correction using all features in the dataset.

Imaging of mouse tissues

Embryonic brains were collected and fixed overnight in 4% PFA, then washed 3 times in 1X PBS. The brains were frozen in OCT and cut 20 µm sections in a cryostat (Leica). The Sections were mounted on glass slides and washed 3 times in 1X PBS. Then were blocked and permeabilized for 1 hour in a blocking buffer containing 0.5% Triton X-100, 1% BSA, and 5% normal donkey serum (Sigma). Then, the sections were incubated with primary antibodies diluted in an antibody dilution buffer containing blocking buffer: PBS (1:1) in a humidified chamber overnight. Next day, the sections were washed 5 times in 1X PBS and after that were incubated with corresponding secondary antibodies in antibody dilution buffer for 2 hours, washed again 5 times 1XPBS. Then mounted with Prolong gold antifade mounting media (Invitrogen). Images were taken using Zeiss 780 upright laser-scanning confocal microscope with a 34-detector array

with a water immersion Zeiss Plan Apochromat 20Å~/1.0, D = 0.17, parfocal length 75 mm (Zeiss). The spectral configuration was set up using the recommended settings from Zen software (Zeiss). Raw images were analyzed using ImageJ (NIH).

TUNEL assay

TUNEL assay was performed on cryosection using the "In Situ Cell Death Detection Kit" (Roche), following the manufacturer instructions.

Edu staining

E14.5 pregnant females were injected with 50mg/Kg Edu 2 hours before sacrifice. Then, embryos were harvested, fixed in 4% PFA. Immunofluorescence was performed on cryosections according to the manufacturer instructions (Click-iT® EdU Imaging Kits – ThermoFisher Scientific).

Mitochondrial extraction and electron transfer chain (ETC) activity

Mitochondria were extracted as reported in (*75*). Cells were lysed in 0.5ml mitochondria lysis buffer (50 mM Tris-HCl, 100 mM KCl, 5 mM $MgCl_2$, 1.8 mM ATP, 1 mM EDTA, pH7.2), supplemented with Protease Inhibitor Cocktail III (Sigma), 1 mM phenylmethylsulfonyl fluoride (PMSF) and 250 mM NaF. Samples were clarified by centrifugation at 650 g for 3 min at 4oC. Supernatants were collected and centrifuged at 13000 g for 5 min at 4oC. The new supernatants, corresponding to the cytosolic fraction, were used for cytosolic ROS measurements. Pellets, containing mitochondria, were washed once with lysis buffer and resuspended in 0.25 ml mitochondria resuspension buffer (250 mM sucrose, 15 mM K_2HPO_4, 2 mM $MgCl_2$, 0.5 mM EDTA). 50 µl aliquots were sonicated and used for the measurement of protein content by the BCA Protein Assay kit (Sigma) and for quality control: 10 µg of each sonicated sample were analyzed by SDS-PAGE and immunoblotting with an anti-porin antibody (Abcam; clone 20B12AF2) to confirm the presence of mitochondrial proteins in the extracts. The remaining 200 µl were used to measure the electron flux from complex I to complex III, taken as an index of the mitochondrial respiratory activity (*75*), 50 µg of non-sonicated mitochondrial samples, isolated as indicated above, were re-suspended in 0.2 ml buffer A (5 mM K_2HPO_4, 5 mM $MgCl_2$, 5% w/v bovine serum albumin, BSA; pH 7.2) to which 0.1 ml buffer B (25% w/v saponin, 50 mM K_2HPO_4, 5 mM $MgCl_2$, 5% w/v BSA, 0.12 mM oxidized cytochrome c, 0.2 mM NaN_3, which blocks complex IV allowing the accumulation of reduced cytochrome c; pH 7.5) was added for 5 min at room temperature. The cytochrome c reduction reaction was started by adding 0.15 mM NADH and was followed for 5 min at 37°C, reading the absorbance at 550 nm by a Packard microplate

reader EL340 (Bio-Tek Instruments, Winooski, VT). The results were expressed as nanomoles of reduced cytochrome c /min/mg mitochondrial proteins.

Adenine nucleotide translocase (ANT) activity

The activity of ANTs was measured fluorimetrically on 250 µg mitochondrial proteins according to (*76*). Results were expressed as µmoles exchanged ATP/mg mitochondrial proteins.

Mitochondrial ATP levels

ATP amounts in mitochondrial extracts were measured with the ATP Bioluminescent Assay Kit (Millipore Sigma), as per manufacturer's instructions. Results were expressed as nmoles ATP/mg mitochondrial proteins.

Tandem Affinity Purification (TAP)

Flp-In T-Rex 293 cells that stably express inducible FLVCR1a cDNA fused to a C-terminal tandem affinity purification (TAP) tag (FLVCR1a-TAP), or the TAP tag alone (empty vector) were generated according to the manufacturer's instructions (Invitrogen). Hygromycin B (Invitrogen) at a concentration of 10 mg/ml was used for selection of stable cell clones. To induce expression doxycycline (Sigma) was administered to the cells at a final concentration of 1 mg/ml for 48 h.

Preparation of pulldown samples for proteomic analysis

The snap-frozen pulldown samples were heated to 95°C for 5 minutes and cooled afterwards until they reached room temperature. Ice-cold acetone was added in a three-fold excess to the samples, which were then stored for protein precipitation at -20°C overnight. Samples with precipitated proteins were centrifuged at 12,000 g at 4°C for 20 minutes. Acetone was removed, and the samples were allowed to dry under the fume hood to evaporate the acetone. 8 M freshly prepared urea (50 µl) was added to the protein pellets to dissolve them. Disulfide bonds were then reduced by the addition of 10 mM TCEP at 37°C for 30 minutes, and free sulfhydryl bonds were alkylated with 15 mM IAA at room temperature (RT) in the dark for 30 minutes. Afterwards, the sample solution was diluted to 1 M urea using 10 mM ABC (ammonium bicarbonate) buffer (pH 7.8), and an in-solution digestion was carried out using 1 µg trypsin (Sigma Gold). Samples were incubated at 37°C overnight. After 15 hours, the reaction was stopped by adding 2 µl of 99% FA (formic acid). The samples were desalted using solid-phase extraction with C18 filter cartridges (Waters), washed with 0.1% TFA, and eluted with 80% acetonitrile. Cleaned samples were dried using a vacuum concentrator and dissolved in 20 µl of 0.1% TFA for mass spectrometry analysis.

Mass spectrometry analysis

All samples were analyzed using an UltiMate 3000 RSLC nano UHPLC coupled to a Thermo Scientific LTQ Orbitrap Velos. The samples were first transferred to a 75 µm x 2 cm, 100 Å, C18 pre column with a flow rate of 20 µl/min for 20 min. followed by a separation on the 75 µm x 50 cm, 100 Å, C18 main column with a flow rate of 250 nl/min and a linear gradient consisting of solution A (99.9% water, 0.1% formic acid) and solution B (84% acetonitrile, 15.9% water, 0.1% formic acid) where the pure gradient length was 100 min (3-38% Solution B). The gradient was applied as follows: 3% B for 20 min, 3-38% for 100 min, followed by 3 wash steps each ranging to 95% buffer B for 3 min. After the last washing step, the instrument was allowed to equilibrate for 20 min at 3% buffer B. The acquisition of MS data was performed in DDA (data dependent acquisition) mode.

Mass Spectrometry data analysis

Data analysis of the acquired label free quantitative MS data was performed using the Progenesis LC-MS software from Nonlinear Dynamics (Newcastle upon Tyne, U.K.). Alignment of MS raw data was conducted by Progenesis, which automatically selected one of the LC-MS files as reference for software-based normalization. Next, peak picking was performed and only features within retention time and m/z windows from 0-90 min and 300-1500 m/z, with charge states +2, +3, and +4 were considered for peptide statistics, analysis of variance (ANOVA). To minimize redundant MS/MS spectra, features with ≤ 5 rank were exported as peak lists which were searched against a concatenated target/decoy version of the human Uniprot database with 20226 target entries, downloaded on 26.10.2017 using Mascot 2.6 (Matrix Science) and X! TANDEM Vengeance (2015.12.15.2) (*77*) with the help of SearchGUI 3.3.11 (*78*). Trypsin with a maximum of two missed cleavages was selected as enzyme. Carbamidomethylation of Cys was set as fixed and oxidation of Met was selected as variable modification. MS and MS/MS tolerances were set to 10 ppm and 0.5 Da, respectively. Combining the search results and filtering the data at a false discovery rate of 1% on the protein, peptide and peptide-spectrum match level was done using PeptideShaker 1.16.36.

Proximity Ligation Assay

Proximity Ligation assays (PLA) were performed on HeLa cells or human primary fibroblasts seeded on a 96 well plate. The assays were performed using a DUOLINK kit (SIGMA Aldrich), following the supplier instructions and with the following antibody associations: rabbit FLVCR1a/mouse IP3R3 (1:50), mouse FLVCR1a /rabbit VDAC1 (1:50), mouse FLVCR1a/rabbit GRP75 (1:50). Negative controls have been made using FLVCR1 mouse or rabbit antibody in pair

with rabbit or mouse antibodies, respectively, recognizing proteins which do not interact with FLVCR1. The following antibody associations were used: rabbit FLVCR1a/mouse PDI (1:50), mouse FLVCR1a/rabbit Atp5i (1:50), mouse FLVCR1a/rabbit Laminin (1:50). To analyze ER-mitochondria contact sites PLA was performed using mouse IP3R3 – rabbit VDAC antibodies pair (1:100). Duolink signal was acquired using the Olympus scanR fluorescence microscope equipped with a equipped with a Uplan S apo 20x and a Hamamatsu ORCA 05G. The scanR Analysis software was used to process and analyze images. Cell were detected using the DAPI signal, for each cell Duolink dots were identified and fluorescence intensity of each dot collected. Duolink signal was then expressed as the integrated fluorescence intensity of all the dots per each cell.

The following antibodies were used: mouse FLVCR1a (Santa Cruz Biotechnology, Dallas, TX USA, catalog n° sc-390100), rabbit FLVCR1a (Proteintech catalog n°26841), VDAC (Abcam catalog n° ab154856), IP3R3 (BD biosciences, catalog n° 610312), GRP75 (Proteintech catalog n°14887), (Abcam, catalog n° ab2792), ATP5i (Abcam, catalog n° ab126181), Lamin A/C (Santa Cruz Biotecnology, catalog n° sc-7292)

Subcellular fractionation

Fractionations were performed as described previously (*79*). IP3R3 (BD biosciences 610312), Vimentin (Abcam, catalog n° ab92547), and VDAC (Abcam ab154856) were used as markers for the ER, cytosol, and pure mitochondria, respectively.

Embryonic neocortical neuroprogenitor cell (NPC) primary cultures

Mouse dorsal telencephalon was dissected from E12.5 brains in DMEM/F12 medium (Invitrogen). Cell suspension was obtained by mechanical dissociation. NSCs from each telencephalon were grown individually as neurospheres in 6 well plates and in DMEM/F12 medium supplemented with 1xN2 and 0.5xB27, 10 ng/ml EGF (Invitrogen) and bFGF (Sigma Aldrich) and 10 mg/ml Insulin (Sigma Aldrich). Two days after the culture start, primary cultures of the same genotype were pooled by two or three in a 10cm dish for further expansion during two to three days. At this stage, neurospheres were pelleted for protein or RNA extraction, or mechanically dissociated for seeding on gelatin-coated dishes, glass coverslips in 24-well plates or IBIDI slides (IBIDI). Attached cells were cultured in DMEM medium (Invitrogen) supplemented with 20% fetal bovine serum and 1mM sodium pyruvate. Cells were then maintained in culture for a maximum of 7 days.

Embryonic neocortical neuroprogenitor cell calcium imaging and quantification

For ratiometric mito-GEM-GECO1 imaging of neuroepithelial cultures, the 405-nm Diode laser of a Leica TCS SP8 confocal scanning system (Leica Microsystems) was used. Emission windows were set to 427-467 nm (blue channel) and 502-537 nm (green channel). Eight-bit digital images were collected from a single optical plane using a 63x HC PL APO CS2 oil-immersion Leica objective (numerical aperture 1.40). Settings for laser intensity, pinhole (1 Airy unit), range property of emission window, electronic zoom, gain and offset of photomultiplicator, field format, scanning speed were optimized initially and held constant throughout the study so that all cells were digitized under the same conditions. Mitochondrial signals of the blue and green channels were segmented; their ratio was calculated and measured using the Analyze Particles command of FIJI/ImageJ (Schindelin et al., 2012; Schneider et al., 2012). In order to evoke Calcium discharge from the Endoplasmic Reticulum and rapid Calcium accumulation inside mitochondria, neuronal progenitor cells (NSCs) were treated with Carbachol at a working concentration of 500µM.

Western Blotting

To assess FLVCR1a expression, cells were lysed by rotation for 30 min at 4 °C in RIPA buffer (150 mM NaCl, 50 mM Tris–HCl pH 7.5, 1% Triton X-100, 0.5% Sodium deoxycholate, 0.1% SDS, 1 mM EDTA). The buffer was freshly supplemented with 1 mM phosphatase inhibitor cocktail (Sigma Aldrich, St. Louis, MO USA, catalog n° P0044), 1 mM PMSF (Sigma Aldrich, St. Louis, MO USA, catalog n° 93482-50ML-F), and protease inhibitor cocktail (La Roche, Basel, CH, catalog n° 04693116001). The cell lysate was clarified by centrifugation for 10 min at 4 °C. Protein concentration in the supernatant was assessed by Bradford assay. For FLVCR1a protein detection, 10 ug of protein extracts was incubated 10 min at 37 °C with 1 uL of PNGase-F from Elizabethkingia meningoseptica (Sigma Aldrich, St. Louis, MO USA, catalog n° P-7367) to remove protein glycosylation. Before loading on 4–15% mini- PROTEAN TGX precast gel (Bio-Rad, Hercules, CA USA, catalog n°4568084), samples were incubated 5 min at 37 °C (FLVCR1) or 5 min at 95 °C (Vinculin, VDAC, IP3R3) in 4 × laemmli buffer freshly supplemented with 8% 2-mercaptoethanol.

The primary antibodies and dilutions are as follows: FLVCR1 (C-4) (Santa Cruz Biotechnology, Dallas, TX USA, catalog n° sc-390100; 1:500); Vinculin (home-made, 1:8000); Anti-myc tag antibody (1:1000 Abcam catalog n°ab9106), VDAC (1:1000, Abcam catalog n°ab154856), IP3R3 (1:2000, BD biosciences catalog n°610312)

Endoplasmic reticulum (ER) - mitochondria contact sites measurement.

Contact sites between ER and mitochondria were analyzed as follows. HeLa cells were transfected using a plasmid containing a mitochondria localization peptide fused with the fluorescent protein RFP (mt-DsRed) and a plasmid containing the ER resident protein Sec61 fused with GFP (Sec61-GFP). Living cells were analyzed for mt-DsRed and Sec61-GFP expression using an Olympus FV3000 confocal microscope equipped with PLAPON60XOSC2 60X oil immersion objective (n.a. 1.4). Colocalization of the two signals was quantified using the ImageJ Colocalization plugin JACOP, upon application of the TOP HAT (BOX) filter. A total of 10 cells per coverslip and 3 coverslips per experiment were analyzed. The results indicated a total of 3 independent experiments (n=3).

Aequorin based Calcium measurements.

All aequorin measurements were performed transfecting cells with the appropriate aequorin chimera targeted to the mitochondria (mtAEQmut) or cytosol (citAEQ), as previously described (*49*). Briefly, cells were seeded onto 13mm glass coverslips and transfected with a mitochondrial or cytosolic targeted Aequorin probe. Before the measurement, cells were incubated with 5 mM coelenterazine for 1.5 hours in a saline buffer supplemented with 1mM CaCl2, and then transferred to the perfusion chamber. Cells were stimulated using an IP3-dependent agent (Histamine) to evoke Calcium discharge from the Endoplasmic Reticulum and rapid Calcium accumulation inside mitochondria. The experiments were terminated by lysing cells with Triton X-100 in a hypotonic calcium-rich solution, thus discharging the remaining aequorin pool. The light signal was collected and calibrated into [Ca2+] values by an algorithm based on the Calcium response curve of aequorin at physiological conditions of pH, [Mg2+], and ionic strength. 5 coverslips per experiment were subjected to the analysis. The results represent a total of 3 independent experiments (n=3).

FRET based calcium measurement.

Single-cell measurements of [Ca2+]m were performed in HeLa cells transfected with 4mtD3cpv. After 36 h, cells were imaged on a Zeiss Axiovert 100TV microscope equipped with a Uplan S Apo 60X oil immersion objective (n.a. 1.35), a Retiga R3 CCD camera (Photometrics) and controlled by METAFLUOR 7.0 Software (Universal Imaging). Emission ratio imaging of the cameleon was accomplished by using a 436DF20 excitation filter, a 450 nm dichroic mirror, and two emission filters (475/40 for ECFP and 535/25 for citrine) controlled by a Lambda 10-2 filter changer (Sutter Instruments). Fluorescence images were background corrected. Exposure times were typically 100 to 200 ms, and ratio images were collected 1 Hz.

Gene silencing and overexpression

FLVCR1a silencing in HeLa cells was performed using a shRNA that specifically downregulates FLVCR1a, without targeting the FLVCR1b isoform (TRC Lentiviral pLKO.1 Human FLVCR1 shRNA set RHS4533-EG28982, clone TRCN0000059599; Dharmacon, Lafayette, CO, USA). For control cells, a pLKO.1 lentiviral vector expressing a scramble (scr) shRNA was used. For FLVCR1a overexpression in HeLa cells the PLVX-pure vector with FLVCR1a-Myc-Tag was used. For control cells, the empty vector was used. Following lentiviral transduction, cells were maintained in selective medium containing 0.002mg/ml puromycin (Puromycin dihydrochloride from Streptomyces alboniger, Sigma-Aldrich, St. Louis, MO USA, catalog n P8833).

Transient MCU overexpression was performed by transfecting human primary fibroblasts with JETOPTIMUS (Polyplus) accordingly to manufacturer instructions. mito-GEM-GECO vector overexpression in Neural progenitor cells (NSCs) was achieved by using JETOPTIMUS (Polyplus) accordingly to manufacturer instructions.

RNA extraction and quantitative real-time PCR analysis

Total RNA was extracted from mouse brain using Purelink RNA mini kit (Thermofisher Scientific, Waltham, MA USA, catalog n 12183018A). Between 500 and 1000ng of total RNA were transcribed into complementary DNA (cDNA) by High-Capacity cDNA Reverse Transcription Kit (Thermofisher Scientific, Waltham, MA USA, catalog n 4368813). Quantitative real-time PCR (qRT-PCR) was performed using gene-specific TaqMan™ Gene Expression Assays (Thermo Fisher Scientific Waltham, MA USA). Primers and probes were designed using the ProbeFinder software (Roche, Basel, CH, https://lifescience.roche.com/en_it/articles/Universal-ProbeLibrary-System-Assay-Design.html; RRID:SCR_014490). For FLVCR1a, specific primers and the probe were designed using Primer Express Software v3.0 (Thermofisher Scientific, Waltham, MA USA, https://www.thermofisher.com/order/catalog/product/4363991/; RRID:SCR_014326). qRT-PCR were performed on a 7300 or 7900 Real Time PCR System (Thermofisher Scientific, Waltham,MAUSA). Transcript abundance, normalized to 18 s mRNA expression is expressed as a fold increase over a calibrator sample.

Exome sequencing and variant calling

For Yale-CMG cohort, exome capture was performed on genomic DNA samples derived from saliva or blood using the NimbleGen SeqCap EZ MedExome Target Enrichment kit (Roche) or the

xGen target capture kit (IDT), followed by 101 or 148 base paired-end sequencing on Illumina platforms as described previously (*12*). Sequence reads were aligned to human reference genome GRCh37/hg19 (*80*) using BWA-MEM. Single nucleotide variants and small indels were called using GATK HaplotypeCaller and FreeBayes and annotated with ANNOVAR. Minor allele frequencies were annotated using the gnomAD and Bravo databases (*81, 82*). For the GeneDx cohort, samples were sequenced and aligned with either SureSelect Human All Exon v4 (Agilent), Clinical Research Exome (Agilent), or xGen Exome Research Panel v1.0 (IDT) and sequenced with either 2x100 or 2x150bp reads on Illumina HiSeq 2000, 2500, 4000, or NovaSeq 6000 as previously described (*83*). Aligned BAM files (GRCh37/hg19) were converted to CRAM format with Samtools version 1.3.1 and indexed. Individual gVCF files were called with GATK v3.7-0 HaplotypeCaller (*80*) in gVCF mode by restricting output regions to plus/minus 50bp of the RefGene primary coding regions. Single sample gVCF files were then combined into multisample gVCF files, with each combined file containing 200 samples. These multi-sample GVCF files were then jointly genotyped using GATK GenotypeGVCFs (*80*). GATK VariantRecalibrator (VQSR) was applied for both SNPs and small INDELs, with known SNPs from 1000 Genomes phase 1 high confidence set and "gold standard" INDELs. Variants in VQSR VCF files were then annotated with ANNOVAR as previously described.

***De novo* calling and filtering.**

DNVs were called as previously described (*84, 85*). DNV calls were filtered to create a high-quality set using the parameters below:

- Read depth (DP) >10 in the proband and both parents
- Variant allele frequency (VAF) > 0.15 in the proband for SNVs and VAF > 0.25 for indels
- > 3 reads supporting the alternative allele
- Genotype Quality (GQ) score > 40
- Log odds of being a true variant versus being false from VQSR > -10 outputted from GATK
- Any variant with a general population frequency above 4×10^{-4} was also excluded based on 1000 Genomes and ExAC variant population frequency data.

- Filter out DNVs called > 4 times in the parental samples in the cohort
- Filter out DNVs with VAF < 0.3 and VQSLOD < 7
- Filter out *de novo* indels > 100bp
- Filter out *de novo* variants not on chromosome X, with a VAF of 1

The impact of non-synonymous variants on protein function was inferred using DeNovoWEST (*84*), which scores all classes of sequence variants on a unified severity scale based on empirically estimated positive predictive pathogenicity values. This software was utilized to assess gene-wise DNV enrichment. Orthogonal analysis with DenovolyzeR (*86*) classified missense variants as "deleterious" (referred to as D-mis) when predicted as deleterious by MetaSVM or with MPC score ≥ 2 (*12, 86, 87*). Inferred loss-of-function (LoF) variants include stop-gains, stop-losses, frameshift-insertions and -deletions, and canonical splice site variants. Protein-damaging variants included LoF and D-mis variants and protein-altering variants comprised of LoF and all missense variants.

Kinship and biological sex determination

The relationship between proband and parents was estimated with pairwise identity-by-descent (IBD) calculation in PLINK (*88*). The IBD sharing between the proband and parents in all trios is between 45% and 55%. Biological sex was determined by EIGENSTRAT, Plink sex check, or relative sequencing coverage of chromosomes X and Y.

References

1. P. Q. Duy *et al.*, Brain ventricles as windows into brain development and disease. *Neuron* **110**, 12-15 (2022).
2. K. T. Kahle, A. V. Kulkarni, D. D. Limbrick, B. C. Warf, Hydrocephalus in children. *Lancet* **387**, 788-799 (2016).
3. H. M. Tully, W. B. Dobyns, Infantile hydrocephalus: a review of epidemiology, classification and causes. *Eur J Med Genet* **57**, 359-368 (2014).
4. M. Kousi, N. Katsanis, The Genetic Basis of Hydrocephalus. *Annu Rev Neurosci* **39**, 409-435 (2016).
5. T. O. Wichmann, H. H. Damkier, M. Pedersen, A Brief Overview of the Cerebrospinal Fluid System and Its Implications for Brain and Spinal Cord Diseases. *Front Hum Neurosci* **15**, 737217 (2021).
6. . (2023).
7. F. Simone, L. Troncone, [Communicating hydrocephalus with normal pressure]. *Riv Neurol* **42**, 54-95 (1972).
8. A. De Backer, Handbook of neurosurgery, 8th edition. *Acta Chir Belg* **116**, 269 (2016).
9. V. Leinonen, R. Vanninen, T. Rauramaa, Cerebrospinal fluid circulation and hydrocephalus. *Handb Clin Neurol* **145**, 39-50 (2017).
10. D. Pang, E. Altschuler, Low-pressure hydrocephalic state and viscoelastic alterations in the brain. *Neurosurgery* **35**, 643-655; discussion 655-646 (1994).
11. J. Riva-Cambrin *et al.*, Impact of ventricle size on neuropsychological outcomes in treated pediatric hydrocephalus: an HCRN prospective cohort study. *J Neurosurg Pediatr*, 1-12 (2021).
12. S. C. Jin *et al.*, Exome sequencing implicates genetic disruption of prenatal neuro-gliogenesis in sporadic congenital hydrocephalus. *Nat Med* **26**, 1754-1765 (2020).
13. P. Q. Duy *et al.*, Impaired neurogenesis alters brain biomechanics in a neuroprogenitor-based genetic subtype of congenital hydrocephalus. *Nat Neurosci* **25**, 458-473 (2022).
14. X. Jiang, J. Nardelli, Cellular and molecular introduction to brain development. *Neurobiol Dis* **92**, 3-17 (2016).
15. T. Namba, W. B. Huttner, Neural progenitor cells and their role in the development and evolutionary expansion of the neocortex. *Wiley Interdiscip Rev Dev Biol* **6**, (2017).
16. J. Bonnefont, P. Vanderhaeghen, Neuronal fate acquisition and specification: time for a change. *Curr Opin Neurobiol* **66**, 195-204 (2021).

17. R. Iwata, P. Vanderhaeghen, Regulatory roles of mitochondria and metabolism in neurogenesis. *Curr Opin Neurobiol* **69**, 231-240 (2021).
18. P. Mao *et al.*, Mesenchymal glioma stem cells are maintained by activated glycolytic metabolism involving aldehyde dehydrogenase 1A3. *Proc Natl Acad Sci U S A* **110**, 8644-8649 (2013).
19. M. Khacho *et al.*, Mitochondrial dysfunction underlies cognitive defects as a result of neural stem cell depletion and impaired neurogenesis. *Hum Mol Genet* **26**, 3327-3341 (2017).
20. W. H. Yoon *et al.*, Loss of Nardilysin, a Mitochondrial Co-chaperone for α-Ketoglutarate Dehydrogenase, Promotes mTORC1 Activation and Neurodegeneration. *Neuron* **93**, 115-131 (2017).
21. N. Journiac *et al.*, Cell Metabolic Alterations due to Mcph1 Mutation in Microcephaly. *Cell Rep* **31**, 107506 (2020).
22. T. Namba *et al.*, Human-Specific ARHGAP11B Acts in Mitochondria to Expand Neocortical Progenitors by Glutaminolysis. *Neuron* **105**, 867-881.e869 (2020).
23. M. Khacho *et al.*, Mitochondrial Dynamics Impacts Stem Cell Identity and Fate Decisions by Regulating a Nuclear Transcriptional Program. *Cell Stem Cell* **19**, 232-247 (2016).
24. C. C. F. Homem *et al.*, Ecdysone and mediator change energy metabolism to terminate proliferation in Drosophila neural stem cells. *Cell* **158**, 874-888 (2014).
25. S. B. Keel *et al.*, A heme export protein is required for red blood cell differentiation and iron homeostasis. *Science* **319**, 825-828 (2008).
26. J. G. Quigley *et al.*, Identification of a human heme exporter that is essential for erythropoiesis. *Cell* **118**, 757-766 (2004).
27. D. Chiabrando *et al.*, The mitochondrial heme exporter FLVCR1b mediates erythroid differentiation. *J Clin Invest* **122**, 4569-4579 (2012).
28. V. Fiorito *et al.*, The heme synthesis-export system regulates the tricarboxylic acid cycle flux and oxidative phosphorylation. *Cell Rep* **35**, 109252 (2021).
29. S. Petrillo *et al.*, Heme accumulation in endothelial cells impairs angiogenesis by triggering paraptosis. *Cell Death Differ* **25**, 573-588 (2018).
30. V. Fiorito, M. Forni, L. Silengo, F. Altruda, E. Tolosano, Crucial role of Flvcr1a in the maintenance of intestinal heme homeostasis. *Antioxid Redox Signal*, (2015).
31. D. Chiabrando *et al.*, Mutations in the Heme Exporter FLVCR1 Cause Sensory Neurodegeneration with Loss of Pain Perception. *PLoS Genet* **12**, e1006461 (2016).
32. M. Philip *et al.*, Heme exporter FLVCR is required for T cell development and peripheral survival. *J Immunol* **194**, 1677-1685 (2015).

33. S. Mercurio *et al.*, Alteration of heme metabolism in a cellular model of Diamond-Blackfan anemia. *Eur J Haematol*, (2015).
34. A. Arjun McKinney, R. Petrova, G. Panagiotakos, Calcium and activity-dependent signaling in the developing cerebral cortex. *Development* **149**, (2022).
35. S. Richards *et al.*, Standards and guidelines for the interpretation of sequence variants: a joint consensus recommendation of the American College of Medical Genetics and Genomics and the Association for Molecular Pathology. *Genet Med* **17**, 405-424 (2015).
36. C. S. Tailor, B. J. Willett, D. Kabat, A putative cell surface receptor for anemia-inducing feline leukemia virus subgroup C is a member of a transporter superfamily. *J Virol* **73**, 6500-6505 (1999).
37. F. Vinchi *et al.*, Heme exporter FLVCR1a regulates heme synthesis and degradation and controls activity of cytochromes P450. *Gastroenterology* **146**, 1325-1338 (2014).
38. S. Mercurio *et al.*, Heme exporter Flvcr1 regulates expansion and differentiation of committed erythroid progenitors by controlling intracellular heme accumulation. *Haematologica*, (2015).
39. A. M. Rajadhyaksha *et al.*, Mutations in FLVCR1 cause posterior column ataxia and retinitis pigmentosa. *Am J Hum Genet* **87**, 643-654 (2010).
40. F. Bertino *et al.*, Heme and sensory neuropathy: insights from novel mutations in the heme exporter feline leukemia virus subgroup C receptor 1. *Pain* **160**, 2766-2775 (2019).
41. S. A. Fietz *et al.*, Transcriptomes of germinal zones of human and mouse fetal neocortex suggest a role of extracellular matrix in progenitor self-renewal. *Proc Natl Acad Sci U S A* **109**, 11836-11841 (2012).
42. A. A. Pollen *et al.*, Molecular identity of human outer radial glia during cortical development. *Cell* **163**, 55-67 (2015).
43. S. Petrillo *et al.*, Endothelial cells require functional FLVCR1a during developmental and adult angiogenesis. *Angiogenesis*, (2023).
44. S. Govindan, P. Oberst, D. Jabaudon, In vivo pulse labeling of isochronic cohorts of cells in the central nervous system using FlashTag. *Nat Protoc* **13**, 2297-2311 (2018).
45. I. S. Shimada, M. Acar, R. J. Burgess, Z. Zhao, S. J. Morrison, Prdm16 is required for the maintenance of neural stem cells in the postnatal forebrain and their differentiation into ependymal cells. *Genes Dev* **31**, 1134-1146 (2017).
46. A. Roy *et al.*, PI3K-Yap activity drives cortical gyrification and hydrocephalus in mice. *Elife* **8**, (2019).
47. J. Janikiewicz *et al.*, Mitochondria-associated membranes in aging and senescence: structure, function, and dynamics. *Cell Death Dis* **9**, 332 (2018).

48. R. Iwata, P. Casimir, P. Vanderhaeghen, Mitochondrial dynamics in postmitotic cells regulate neurogenesis. *Science* **369**, 858-862 (2020).
49. M. Bonora *et al.*, Subcellular calcium measurements in mammalian cells using jellyfish photoprotein aequorin-based probes. *Nat Protoc* **8**, 2105-2118 (2013).
50. R. Rizzuto *et al.*, Close contacts with the endoplasmic reticulum as determinants of mitochondrial Ca2+ responses. *Science* **280**, 1763-1766 (1998).
51. M. Castori *et al.*, Posterior column ataxia with retinitis pigmentosa coexisting with sensory-autonomic neuropathy and leukemia due to the homozygous p.Pro221Ser FLVCR1 mutation. *Am J Med Genet B Neuropsychiatr Genet* **174**, 732-739 (2017).
52. M. Bonora *et al.*, ATP synthesis and storage. *Purinergic Signal* **8**, 343-357 (2012).
53. T. Namba, J. Nardelli, P. Gressens, W. B. Huttner, Metabolic Regulation of Neocortical Expansion in Development and Evolution. *Neuron* **109**, 408-419 (2021).
54. A. Britzolaki, J. Saurine, E. Flaherty, C. Thelen, P. M. Pitychoutis, The SERCA2: A Gatekeeper of Neuronal Calcium Homeostasis in the Brain. *Cell Mol Neurobiol* **38**, 981-994 (2018).
55. A. L. Allocco *et al.*, Inhibition of Heme Export and/or Heme Synthesis Potentiates Metformin Anti-Proliferative Effect on Cancer Cell Lines. *Cancers (Basel)* **14**, (2022).
56. D. Chiabrando *et al.*, Expression and purification of the heme exporter FLVCR1a. *Protein Expr Purif* **172**, 105637 (2020).
57. R. K. Donegan, C. M. Moore, D. A. Hanna, A. R. Reddi, Handling heme: The mechanisms underlying the movement of heme within and between cells. *Free Radic Biol Med* **133**, 88-100 (2019).
58. X. Yuan *et al.*, Regulation of intracellular heme trafficking revealed by subcellular reporters. *Proc Natl Acad Sci U S A* **113**, E5144-5152 (2016).
59. I. G. Chambers, M. M. Willoughby, I. Hamza, A. R. Reddi, One ring to bring them all and in the darkness bind them: The trafficking of heme without deliverers. *Biochim Biophys Acta Mol Cell Res* **1868**, 118881 (2021).
60. D. Chiabrando, F. Vinchi, V. Fiorito, S. Mercurio, E. Tolosano, Heme in pathophysiology: a matter of scavenging, metabolism and trafficking across cell membranes. *Front Pharmacol* **5**, 61 (2014).
61. D. Chiabrando, V. Fiorito, S. Petrillo, E. Tolosano, Unraveling the Role of Heme in Neurodegeneration. *Front Neurosci* **12**, 712 (2018).
62. C. Wiel *et al.*, BACH1 Stabilization by Antioxidants Stimulates Lung Cancer Metastasis. *Cell* **178**, 330-345.e322 (2019).

63. V. Gkini, T. Namba, Glutaminolysis and the Control of Neural Progenitors in Neocortical Development and Evolution. *Neuroscientist*, 10738584211069060 (2022).
64. P. Kalailingam *et al.*, Deficiency of MFSD7c results in microcephaly-associated vasculopathy in Fowler syndrome. *J Clin Invest* **130**, 4081-4093 (2020).
65. N. Santander *et al.*, Lack of Flvcr2 impairs brain angiogenesis without affecting the blood-brain barrier. *J Clin Invest* **130**, 4055-4068 (2020).
66. E. Meyer *et al.*, Mutations in FLVCR2 are associated with proliferative vasculopathy and hydranencephaly-hydrocephaly syndrome (Fowler syndrome). *Am J Hum Genet* **86**, 471-478 (2010).
67. Y. Li *et al.*, MFSD7C switches mitochondrial ATP synthesis to thermogenesis in response to heme. *Nat Commun* **11**, 4837 (2020).
68. J. Rönkkö *et al.*, Dominant mutations in ITPR3 cause Charcot-Marie-Tooth disease. *Ann Clin Transl Neurol* **7**, 1962-1972 (2020).
69. A. Lischka *et al.*, Genetic pain loss disorders. *Nat Rev Dis Primers* **8**, 41 (2022).
70. M. Krols *et al.*, Sensory-Neuropathy-Causing Mutations in ATL3 Cause Aberrant ER Membrane Tethering. *Cell Rep* **23**, 2026-2038 (2018).
71. R. Rizzuto, M. Brini, P. Pizzo, M. Murgia, T. Pozzan, Chimeric green fluorescent protein as a tool for visualizing subcellular organelles in living cells. *Curr Biol* **5**, 635-642 (1995).
72. M. Montero *et al.*, Chromaffin-cell stimulation triggers fast millimolar mitochondrial Ca2+ transients that modulate secretion. *Nat Cell Biol* **2**, 57-61 (2000).
73. L. Song *et al.*, STAB: a spatio-temporal cell atlas of the human brain. *Nucleic Acids Res* **49**, D1029-D1037 (2021).
74. T. Stuart *et al.*, Comprehensive Integration of Single-Cell Data. *Cell* **177**, 1888-1902.e1821 (2019).
75. I. C. Salaroglio *et al.*, Mitochondrial ROS drive resistance to chemotherapy and immune-killing in hypoxic non-small cell lung cancer. *J Exp Clin Cancer Res* **41**, 243 (2022).
76. H. Kawamata, A. A. Starkov, G. Manfredi, C. Chinopoulos, A kinetic assay of mitochondrial ADP-ATP exchange rate in permeabilized cells. *Anal Biochem* **407**, 52-57 (2010).
77. T. Muth, M. Vaudel, H. Barsnes, L. Martens, A. Sickmann, XTandem Parser: an open-source library to parse and analyse X!Tandem MS/MS search results. *Proteomics* **10**, 1522-1524 (2010).
78. M. Vaudel, H. Barsnes, F. S. Berven, A. Sickmann, L. Martens, SearchGUI: An open-source graphical user interface for simultaneous OMSSA and X!Tandem searches. *Proteomics* **11**, 996-999 (2011).

79. M. R. Wieckowski, C. Giorgi, M. Lebiedzinska, J. Duszynski, P. Pinton, Isolation of mitochondria-associated membranes and mitochondria from animal tissues and cells. *Nat Protoc* **4**, 1582-1590 (2009).
80. A. McKenna *et al.*, The Genome Analysis Toolkit: a MapReduce framework for analyzing next-generation DNA sequencing data. *Genome Res* **20**, 1297-1303 (2010).
81. K. J. Karczewski *et al.*, The mutational constraint spectrum quantified from variation in 141,456 humans. *Nature* **581**, 434-443 (2020).
82. D. Taliun *et al.*, Sequencing of 53,831 diverse genomes from the NHLBI TOPMed Program. *Nature* **590**, 290-299 (2021).
83. K. Retterer *et al.*, Clinical application of whole-exome sequencing across clinical indications. *Genet Med* **18**, 696-704 (2016).
84. J. Kaplanis *et al.*, Evidence for 28 genetic disorders discovered by combining healthcare and research data. *Nature* **586**, 757-762 (2020).
85. N. S. Diab *et al.*, Analysis workflow to assess. *STAR Protoc* **2**, 100383 (2021).
86. J. S. Ware, K. E. Samocha, J. Homsy, M. J. Daly, Interpreting de novo Variation in Human Disease Using denovolyzeR. *Curr Protoc Hum Genet* **87**, 7.25.21-27.25.15 (2015).
87. A. J. Kundishora *et al.*, Multiomic analyses implicate a neurodevelopmental program in the pathogenesis of cerebral arachnoid cysts. *Nat Med* **29**, 667-678 (2023).
88. S. Purcell *et al.*, PLINK: a tool set for whole-genome association and population-based linkage analyses. *Am J Hum Genet* **81**, 559-575 (2007).

Figures

A

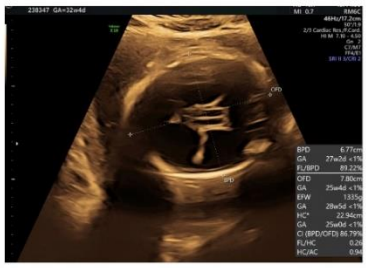

B

Ultrasound findings (32+4 days) last period 05/09/2020, calculated date of birth 02/13/2021:		
Biparietal diameter	67.7 mm	
Front occipital diameter	78.0 mm	
Head circumference	229.4 mm	
Transcerebellar diameter	25.1 mm	
Nose bone can be displayed		
Abdominal transverse diameter	75.4 mm	
Abdomen circumference	244.7 mm	
Humerus	52.8 mm	
Radius	45.0 mm	
Ulna	50.8 mm	
Femur length	60.4 mm	
Tibia	50.1 mm	
Fibula	50.1 mm	
Weight estimate (Hadlock BPD-KU-AU-FL)	1335 g <3rd percent	
Heart action positive. Child movements hardly any child movements. Skull position; Amniotic fluid: upper norm; Placenta: posterior wall. Grading grade 0. Placental structure: normal. Ultrasound machine: GE Voluson E10. Examination method: transabdominal sonography, color Doppler, fetal echocardiography, pW Doppler. Examination conditions: restricted due to contractions. Singleton pregnancy. Fetal measurements (shown at normal mean and 5th / 95th percentile)		

C

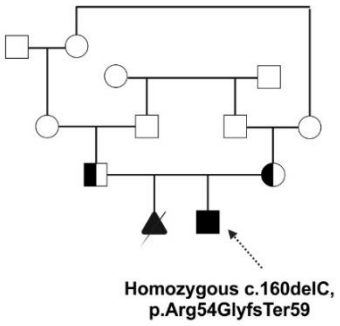

D

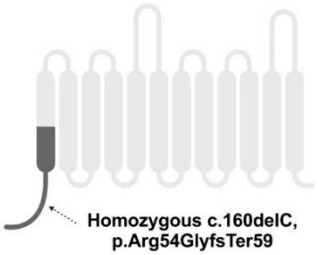

Figure 1. *FLVCR1* inactivating mutations cause congenital hydrocephalus in humans.

(A) Sonographic examinations of 32 + 4 weeks of pregnancy showing extreme microcephaly with anechoic skull and no evidence of cerebral tissue. **(B)** Ultrasound findings (32+4 days) last period of pregnancy. **(C)** Family tree of the affected fetus born by two consanguineous parents. **(D)** FLVCR1a protein model. Predicted p.Arg54GlyfsTer59 protein is highlighted in grey.

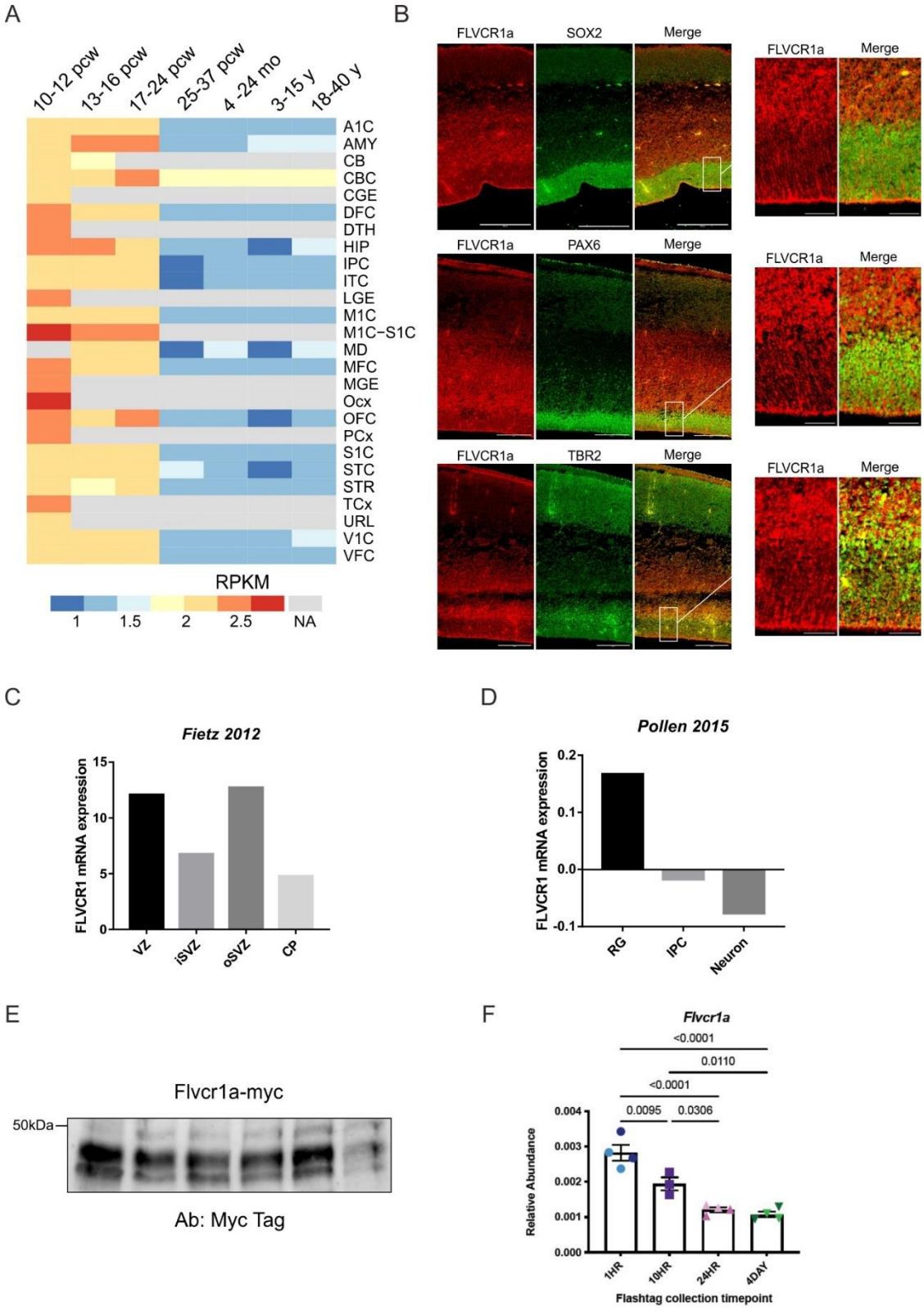
A
10-12 pcw
13-16 pcw
17-24 pcw
25-37 pcw
4 -24 mo
3-15 y
18-40 y
A1C
AMY
CB
CBC
CGE
DFC
DTH
HIP
IPC
ITC
LGE
M1C
M1C−S1C
MD
MFC
MGE
Ocx
OFC
PCx
S1C
STC
STR
TCx
URL
V1C
VFC
RPKM
1
1.5
2
2.5
NA
B
FLVCR1a
SOX2
Merge
FLVCR1a
Merge
FLVCR1a
PAX6
Merge
FLVCR1a
Merge
FLVCR1a
TBR2
Merge
FLVCR1a
Merge
C
Fietz 2012
FLVCR1 mRNA expression
15
10
5
0
VZ
iSVZ
oSVZ
CP
D
Pollen 2015
FLVCR1 mRNA expression
0.2
0.1
0.0
-0.1
RG
IPC
Neuron
E
Flvcr1a-myc
50kDa
Ab: Myc Tag
F
Flvcr1a
<0.0001
0.0110
<0.0001
0.0095
0.0306
Relative Abundance
0.004
0.003
0.002
0.001
0.000
1HR
10HR
24HR
4DAY
Flashtag collection timepoint

Figure 2. *FLVCR1a* is highly expressed in the human and mouse developing brain. (A) *FLVCR1a* expression data from developing human brain extracted from the Dataset GSE25219 of the Human BrainSpan Atlas. This dataset consists of RNA sequencing and exon microarrays obtained at sequential developmental stages of the human brain. Heat map indicates low (blue) and high (red) expression values. Grey colour represents that no data are available. PCW, Post Conception weeks; A1C, auditory cortex; AMY, amygdala; CBC, cerebellar cortex; DFC, dorsolateral prefrontal cortex; HIP, hippocampus; IPC, posterior inferior parietal cortex; ITC, inferior temporal cortex; M1C, primary motor cortex; MD, mediodorsal nucleus of the thalamus; MFC, medial pre-frontal cortex; OFC, orbital prefrontal cortex; S1C, primary somatosensory cortex; STC, superior temporal cortex; STR, striatum; V1C, primary visual cortex; VFC, ventrolateral prefrontal cortex. **(B)** FLVCR1a staining (red) in 11 Post Conception Weeks (PCW) human brain sections shows expression in radial glial cells (RGCs, green, PAX6 and SOX2) and intermediate progenitors (IPs, TBR2). *Scale bar: 500µm*. Magnified images of the insets on the left are shown on the right. *Scale bar: 100 µm*. **(C)** *FLVCR1a* expression in human ventricular zone (VZ), inner subventricular zone (iSVZ), outer subventricular zone (oSVZ) and cortical plate (CP) from the Fietz et. al dataset (*41*). **(D)** *FLVCR1a* expression in radial glia (RGCs), intermediate progenitors (IPs) and mature neurons from the Pollen et. al dataset (*42*). **(E)** Western blot analysis of embryo brains from E12.5 to 18.5, P2 brains and adult brains from Flvcr1-myc mice. Adult mice refer to 3 months old mice. An antibody against the Myc-Tag was used to visualize the expression of endogenous Flvcr1a. A representative image is shown. **(F)** Expression of *Flvcr1a* in “Flashtag”-labelled cell populations in the developing mouse cortex. The different isolation time points correspond to specific populations as follows: 1hr, radial glia (RGCs); 10hr, intermediate progenitors (IPs); 24hr, newborn neurons; and 4 days neurons.

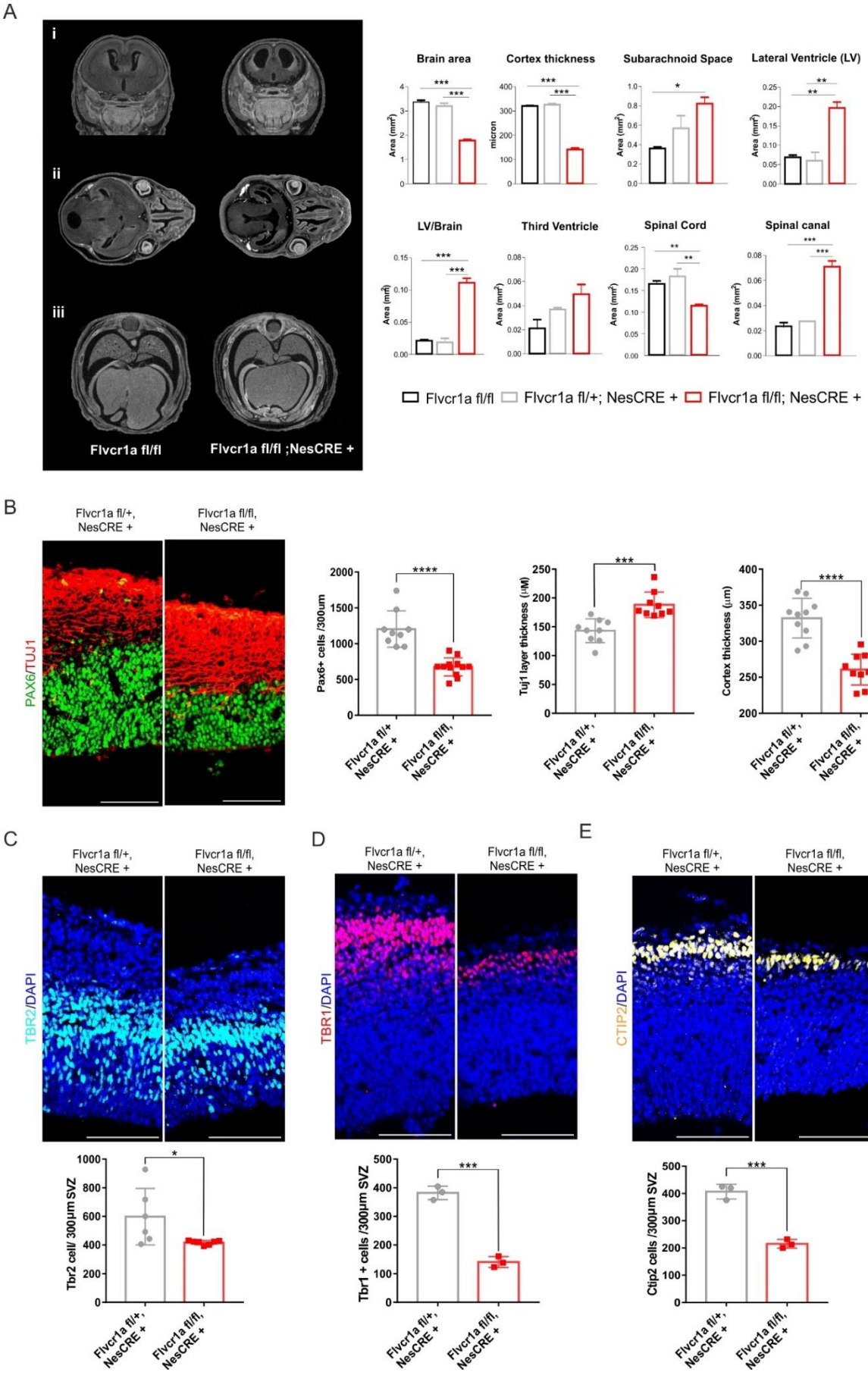
A
i
ii
iii
Flvcr1a fl/fl
Flvcr1a fl/fl ;NesCRE +
Brain area
Cortex thickness
Subarachnoid Space
Lateral Ventricle (LV)
LV/Brain
Third Ventricle
Spinal Cord
Spinal canal
Area (mm²)
micron
Flvcr1a fl/fl
Flvcr1a fl/+; NesCRE +
Flvcr1a fl/fl; NesCRE +
B
Flvcr1a fl/+, NesCRE +
Flvcr1a fl/fl, NesCRE +
PAX6/TUJ1
Pax6+ cells /300um
Tuj1 layer thickness (μM)
Cortex thickness (μm)
C
TBR2/DAPI
Tbr2 cell/ 300μm SVZ
D
TBR1/DAPI
Tbr1 + cells /300μm SVZ
E
CTIP2/DAPI
Ctip2 cells /300μm SVZ

Figure 3. Loss of *Flvcr1a* in neural progenitors causes microcephaly and hydrocephalus in mice, resembling the human syndrome. (A) X-ray computed micro-tomography (micro-CT) analyses were performed on *Flvcr1a*$^{fl/fl}$;NesCRE+ mutant and *Flvcr1afl/+*;NesCRE+ and *Flvcr1afl/fl* control embryos at E18.5. The area of the brain, subarachnoid space, ventricles, spinal cord, and spinal canal, as well as the cortical thickness, were quantified with ImageJ Software. (N=3; One-way ANOVA, *=P<0.05; **=P<0.005; ***=P<0.001.) **(B)** Immunostaining of PAX6 (RGCs) and TUJ1 (cortical neurons) in sections of *Flvcr1a*$^{fl/fl}$;NesCRE+ mutant and *Flvcr1a*$^{fl/+}$;NesCRE+ mouse cortex at E14.5. Each dot represents the mean of 3 images quantified from each animal. n=3. Scale bar=100µm. **(C)** Immunostaining of TBR2 (IPs) in *Flvcr1a*$^{fl/fl}$;NesCRE+ mutant and *Flvcr1a*$^{fl/+}$;NesCRE+ E14.5 mouse cortex. DAPI (blue) was used as a nuclear marker. Each dot represents the mean of 3 images quantified from each animal. n=3. Scale bar=100µm. **(D)** Immunostaining of TBR1 (cortical neurons) in *Flvcr1a*$^{fl/fl}$;NesCRE+ mutant and *Flvcr1a*$^{fl/+}$;NesCRE+ E14.5 mouse cortex. DAPI (blue) was used as a nuclear marker. Each dot corresponds to the mean of three different measurements. **(E)** Immunostaining of CTIP2 (cortical neurons) in *Flvcr1a*$^{fl/fl}$;NesCRE+ mutant and *Flvcr1a*$^{fl/+}$;NesCRE+ E14.5 mouse cortex. DAPI (blue) was used as a nuclear marker. Each dot represents the mean of 3 images quantified from each animal. n=3. Scale bar=100µm. (T-Test; *=P<0.05; **=P<0.01; ***=P<0.001; ****=P<0.0001.)

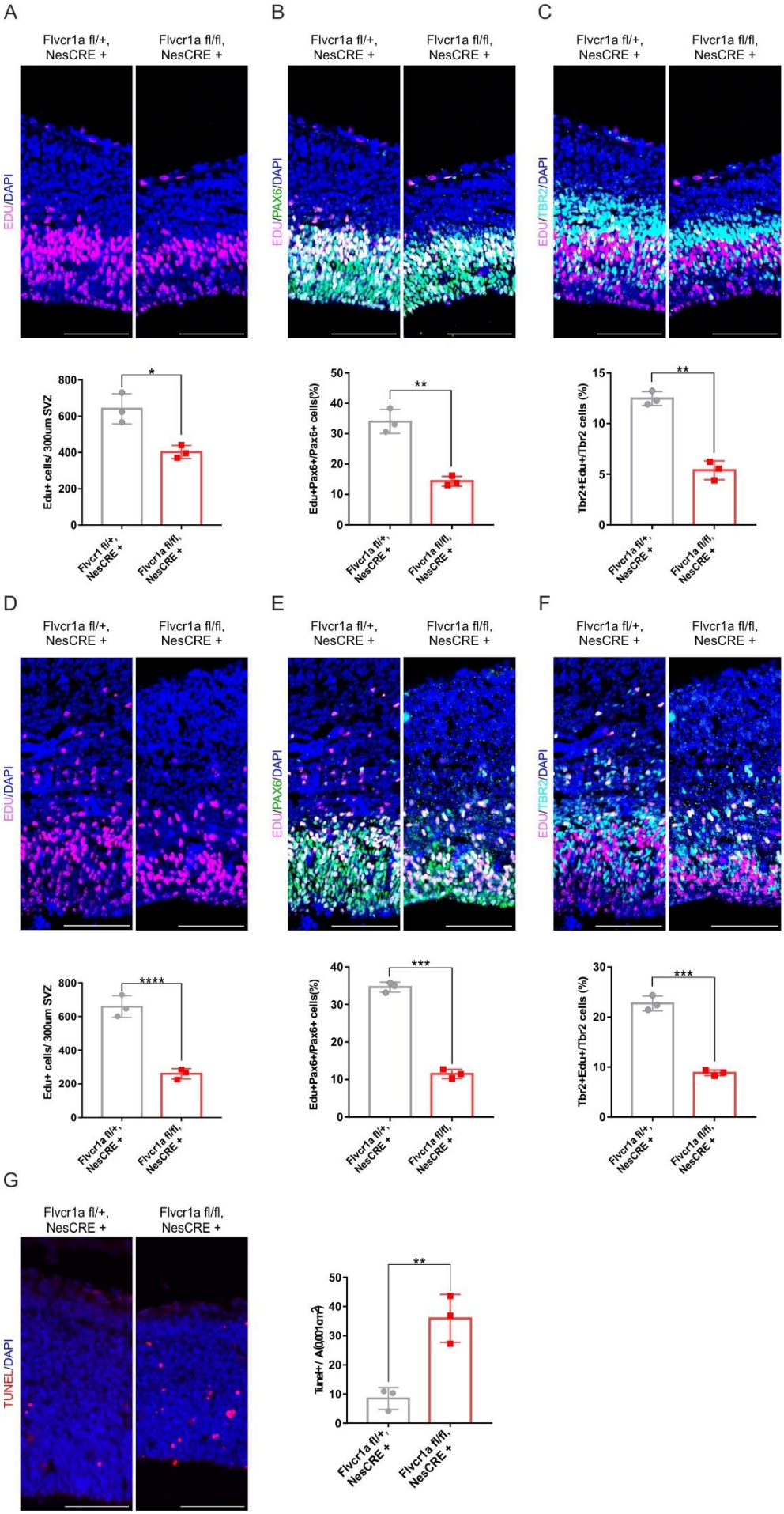
A
B
C
D
E
F
G
Flvcr1a fl/+, NesCRE +
Flvcr1a fl/fl, NesCRE +
EDU/DAPI
EDU/PAX6/DAPI
EDU/TBR2/DAPI
TUNEL/DAPI
Edu+ cells/ 300um SVZ
Edu+Pax6+/Pax6+ cells(%)
Tbr2+Edu+/Tbr2 cells (%)
Tunel+/ A(0.001cm2)
*
**
***
****

Figure 4. *Flvcr1a* loss severely impacts neural progenitor proliferation and survival. (A) EdU staining of E14.5 *Flvcr1a*$^{fl/fl}$;NesCRE+ mutant and *Flvcr1a*$^{fl/+}$;NesCRE+ cortex. DAPI (blue) was used as a nuclear marker. Each dot represents the mean of 3 images quantified from each animal. n=3. Scale bar=100µm. **(B)** EdU and PAX6 co-staining of E14.5 *Flvcr1a*$^{fl/fl}$;NesCRE+ mutant and *Flvcr1a*$^{fl/+}$;NesCRE+ cortex. DAPI (blue) was used as a nuclear marker. Each dot represents the mean of 3 images quantified from each animal. n=3. Scale bar=100µm. **(C)** EdU and TBR2 co-staining of E14.5 *Flvcr1a*$^{fl/fl}$;NesCRE+ mutant and *Flvcr1a*$^{fl/+}$;NesCRE+ control cortex. DAPI (blue) was used as a nuclear marker. Each dot represents the mean of 3 images quantified from each animal. n=3. Scale bar=100µm. **(D)** EdU staining of E16.5 *Flvcr1a*$^{fl/fl}$;NesCRE+ mutant and *Flvcr1a*$^{fl/+}$;NesCRE+ cortex. DAPI (blue) was used as a nuclear marker. **(E)** EdU and PAX6 co-staining of E16.5 *Flvcr1a*$^{fl/fl}$;NesCRE+ mutant and *Flvcr1a*$^{fl/+}$;NesCRE+ cortex. DAPI (blue) was used as a nuclear marker. Each dot represents the mean of 3 images quantified from each animal. n=3. Scale bar=100µm. **(F)** EdU and TBR2 co-staining of E16.5 *Flvcr1a*$^{fl/fl}$;NesCRE+ mutant and *Flvcr1a*$^{fl/+}$;NesCRE+ cortex. DAPI (blue) was used as a nuclear marker. Each dot represents the mean of 3 images quantified from each animal. n=3. Scale bar=100µm. **(G)** TUNEL assay of E14.5 *Flvcr1a*$^{fl/fl}$;NesCRE+ mutant and *Flvcr1a*$^{fl/+}$;NesCRE+ cortex. DAPI (blue) was used as a nuclear marker. Scale bar=100µm. (T-Test; *=P<0.05; **=P<0.01; ***=P<0.001; ****=P<0.0001.

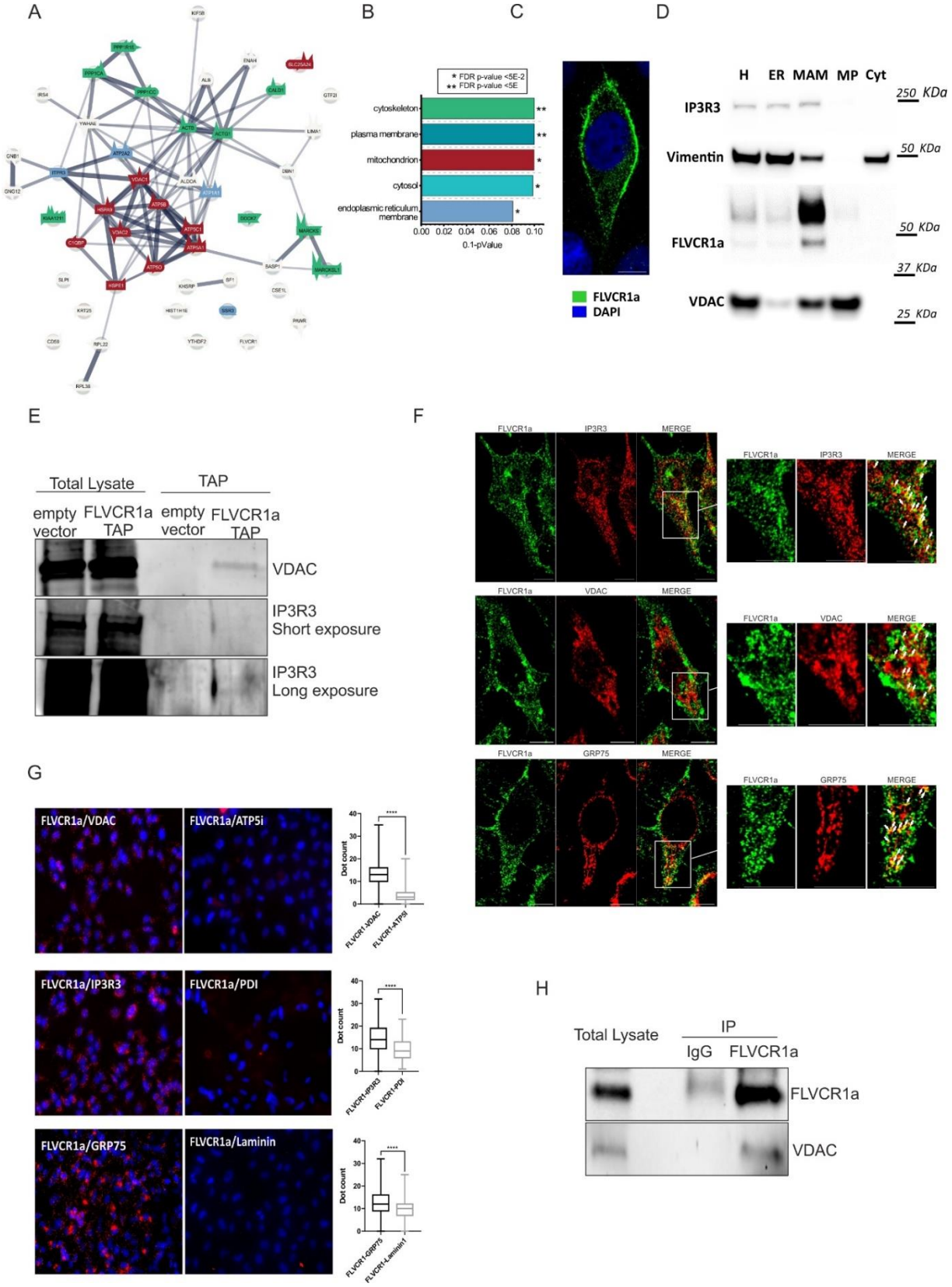
A
B
C
D
* FDR p-value <5E-2
** FDR p-value <5E
cytoskeleton
plasma membrane
mitochondrion
cytosol
endoplasmic reticulum membrane
0.1-pValue
FLVCR1a
DAPI
H ER MAM MP Cyt
IP3R3
Vimentin
FLVCR1a
VDAC
250 KDa
50 KDa
50 KDa
37 KDa
25 KDa
E
Total Lysate
TAP
empty vector
FLVCR1a TAP
empty vector
FLVCR1a TAP
VDAC
IP3R3 Short exposure
IP3R3 Long exposure
F
FLVCR1a
IP3R3
MERGE
VDAC
GRP75
G
FLVCR1a/VDAC
FLVCR1a/ATP5i
FLVCR1a/IP3R3
FLVCR1a/PDI
FLVCR1a/GRP75
FLVCR1a/Laminin
Dot count
H
Total Lysate
IP
IgG
FLVCR1a
FLVCR1a
VDAC

Figure 5. FLVCR1a interacts with the IP3R3-VDAC-GRP75 complex at MAMs. (A) STRING analysis of the top 50 FLVCR1a interactors showing a network of proteins located at mitochondria and endoplasmic reticulum (ER). **(B)** Gene ontology (GO) term analysis for subcellular compartments of the top 50 FLVCR1a interactors, showing mitochondria and ER compartments enrichment. **(C)** Immunofluorescence analysis of FLVCR1a protein localization (green) in HeLa cells. DAPI (Blue) was used as a nuclear staining. Scale bar=10µm. **(D)** Subcellular fractionation of THP1 cells showing FLVCR1a enrichment in the MAMs fraction. **(E)** TAP purification of FLVCR1a followed by western blot of endogenous VDAC and IP3R3 confirms their interaction. **(F)** Immunofluorescence staining for FLVCR1a (red) and VDAC1 (green) or IP3R3 (green), or GRP75 (green) confirms intracellular colocalization in HeLa cells (white arrows). Scale bar=10µm. **(G)** Proximity Ligation Assay (PLA) was performed in HeLa cells using the FLVCR1a and VDAC1 antibodies (FLVCR1a-ATP5i pair was used as a negative control), or the FLVCR1a and IP3R3 antibodies (FLVCR1a-PDI pair was used as a negative control), or the FLVCR1a and GRP75 antibodies (FLVCR1a-Laminin pair was used as a negative control). **(H)** Immunoprecipitation of FLVCR1a followed by western blot for VDAC confirmed endogenous protein interaction in HEK293 cells.

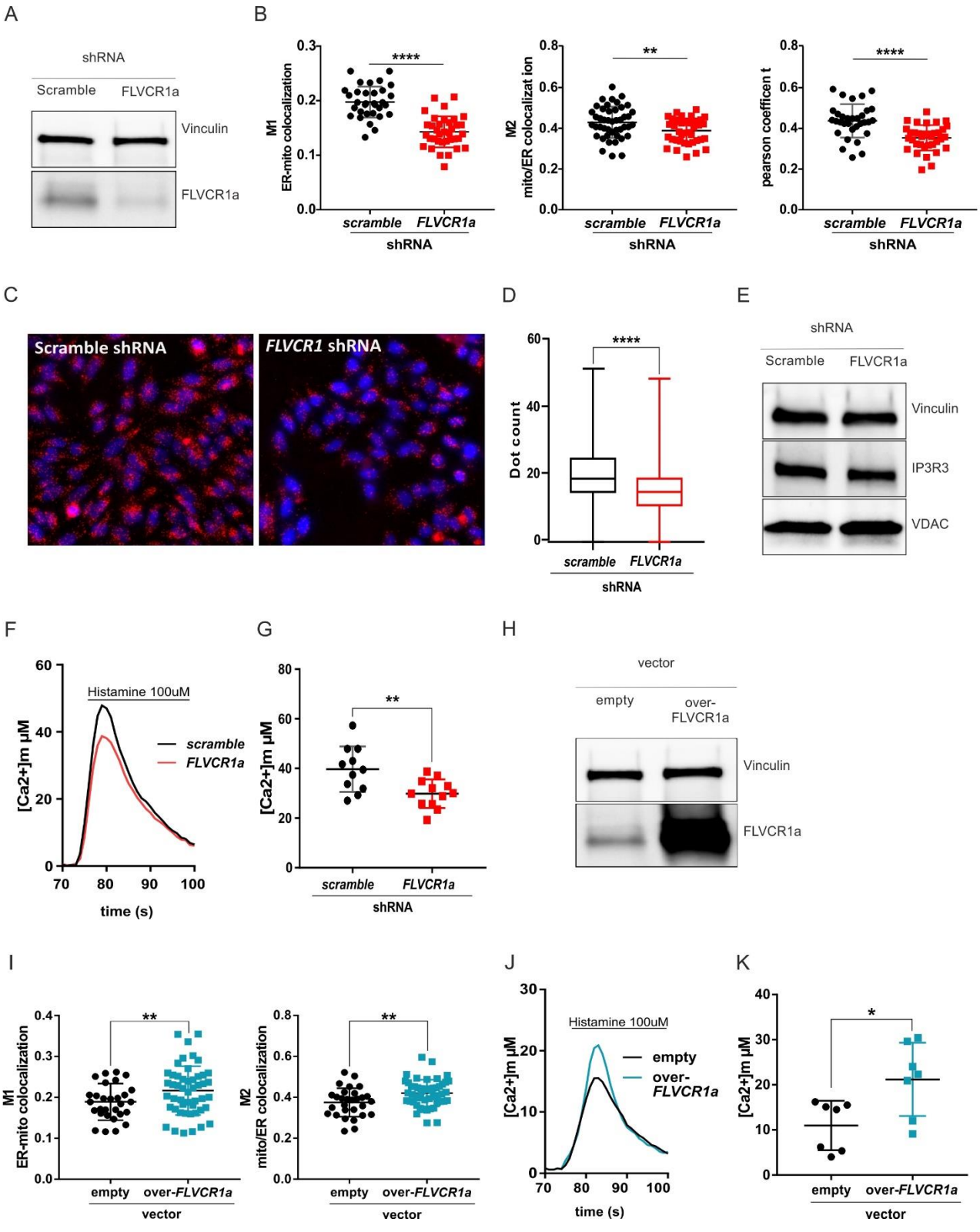
A
shRNA
Scramble
FLVCR1a
Vinculin
FLVCR1a
B
M1 ER-mito colocalization
****
scramble
FLVCR1a
shRNA
M2 mito/ER colocalizat ion
**
scramble
FLVCR1a
shRNA
pearson coefficent t
****
scramble
FLVCR1a
shRNA
C
Scramble shRNA
FLVCR1 shRNA
D
Dot count
****
scramble
FLVCR1a
shRNA
E
shRNA
Scramble
FLVCR1a
Vinculin
IP3R3
VDAC
F
Histamine 100uM
scramble
FLVCR1a
[Ca2+]m µM
time (s)
G
[Ca2+]m µM
**
scramble
FLVCR1a
shRNA
H
vector
empty
over-FLVCR1a
Vinculin
FLVCR1a
I
M1 ER-mito colocalization
**
empty
over-FLVCR1a
vector
M2 mito/ER colocalization
**
empty
over-FLVCR1a
vector
J
Histamine 100uM
empty
over-FLVCR1a
[Ca2+]m µM
time (s)
K
[Ca2+]m µM
*
empty
over-FLVCR1a
vector

Figure 6. FLVCR1a is critical for ER-mitochondria association and ER to mitochondria calcium influx. (A) Representative western blot showing FLVCR1a protein levels upon FLVCR1a downregulation using shRNA. A scramble shRNA was used as a control. **(B)** Quantification of Manders coefficients (M1 and M2) and Pearson correlation coefficient on confocal images of HeLa cells expressing mt-DsRed and sec61-GFP, following transfection with scramble or FLVCR1a shRNA. **(C)** ER-mitochondria contact sites in HeLa cells upon FLVCR1a downregulation quantified by PLA. **(D)** Dot count quantification of PLA experiment showing reduced ER-mitochondria contact sites upon downregulation of FLVCR1a. **(E)** Western blot analysis of VDAC and IP3R3 proteins in HeLa cells showing no differences in protein abundance upon FLVCR1a downregulation. A representative image is shown. **(F)** Mitochondrial calcium uptake measured as calcium (Ca2+) responses to an agonist stimulation (100 µM Histamine) in HeLa cells expressing a mitochondrial aequorin-based probe. Representative calcium traces are shown. **(G)** Quantification of peak mitochondrial calcium amplitude in HeLa cells upon agonist stimulation. Each dot represents a single replicate of 5 technical replicates from three independent experiments. **(H)** Representative western blot showing FLVCR1a protein levels upon FLVCR1a-Myc-Tag stable overexpression (over-FLVCR1a). The same empty vector (PLVX-puro) was used as a control. **(I)** Quantification of Manders coefficients (M1 and M2) on confocal images of HeLa cells expressing mito-RFP and sec61-GFP following transfection with empty or over-FLVCR1a vectors. **(J)** Mitochondrial calcium uptake measured as calcium responses to an agonist stimulation (100 µM Histamine) in HeLa cells expressing a mitochondrial aequorin-based probe. Representative calcium traces are shown. **(K)** Quantification of peak mitochondrial calcium amplitude in HeLa cells upon agonist stimulation from two independent experiments. (T test *=P<0.05; **=P<0.01; ***=P<0.001; ****=P<0.0001.)

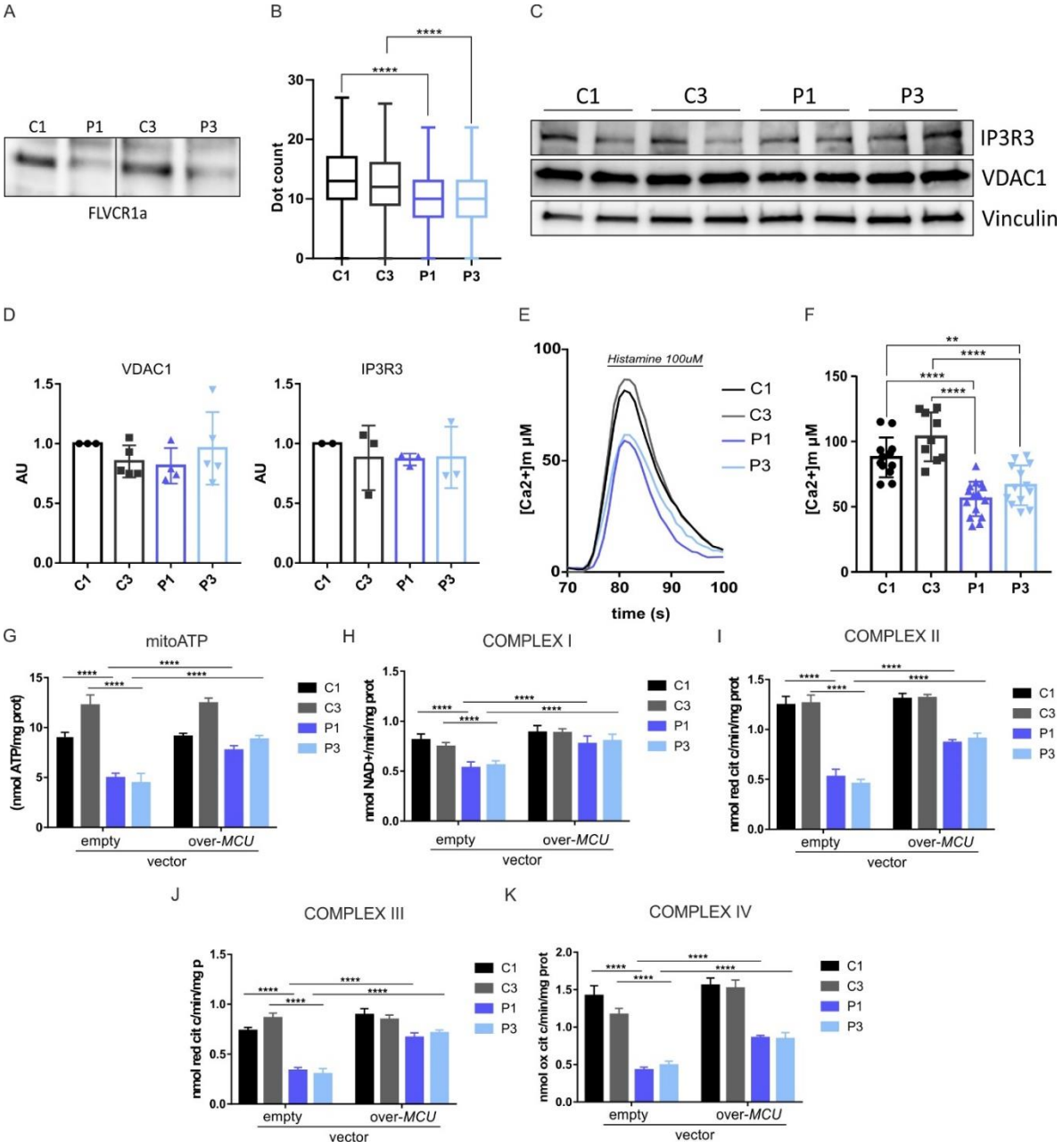
A
C1
P1
C3
P3
FLVCR1a
B
Dot count
C1
C3
P1
P3
C
C1
C3
P1
P3
IP3R3
VDAC1
Vinculin
D
VDAC1
IP3R3
AU
E
Histamine 100uM
[Ca2+]m µM
time (s)
F
[Ca2+]m µM
G
mitoATP
(nmol ATP/mg prot)
empty
over-MCU
vector
H
COMPLEX I
nmol NAD+/min/mg prot
I
COMPLEX II
nmol red cit c/min/mg prot
J
COMPLEX III
nmol red cit c/min/mg p
K
COMPLEX IV
nmol ox cit c/min/mg prot

Figure 7. Reduced ER-mitochondria membrane tethering and impaired mitochondrial calcium uptake in human cells carrying FLVCR1a mutations. (A) Representative western blot depicting FLVCR1a abundance in patient-derived fibroblasts and control subject fibroblasts. **(B)** Decreased ER-mitochondria contact sites in patient-derived fibroblasts carrying mutations in FLVCR1a, quantified by PLA. **(C)** Western blot of VDAC and IP3R3 proteins in control and patient fibroblasts. A representative image is shown. **(D)** Western blot quantification of protein relative abundance. Each dot represents a single replicate of three independent experiments. **(E)** Mitochondrial calcium uptake measured as calcium responses to agonist stimulation (100 µM Histamine) in primary human fibroblasts. Representative calcium traces are shown. **(F)** Quantification of peak mitochondrial calcium amplitude in primary human fibroblasts upon agonist stimulation, from three independent experiments. **(G)** ATP levels measured by a bioluminescence assay in patients and controls derived fibroblasts, in normal conditions or upon overexpression of the low affinity mitochondrial calcium uniporter (MCU). Results are shown as nmoles ATP/mg of mitochondrial proteins. (One-way ANOVA. *=P<0.05; **=P<0.005; ****=P<0.001.). **(H)** Activity of the mitochondrial electron transport chain (ETC) complex I in patient-derived fibroblasts in normal conditions or upon overexpression of the mitochondrial calcium uniporter (MCU). Results are shown as nmoles of NAD+/min/mg of mitochondrial protein. **(I)** Activity of the mitochondrial electron transport chain (ETC) complex II in patients and controls derived fibroblasts, in normal conditions or upon overexpression of the mitochondrial calcium uniporter (MCU). Results are shown as nmoles reduced cytochrome c/min/mg of mitochondrial protein. **(J)** Activity of the mitochondrial electron transport chain (ETC) complex III in patients and controls derived fibroblasts, in normal conditions or upon overexpression of the mitochondrial calcium uniporter (MCU). Results are shown as nmoles reduced cytochrome c/min/mg of mitochondrial protein. **(K)** Activity of the mitochondrial electron transport chain (ETC) complex IV in patients and controls derived fibroblasts, in normal conditions or upon overexpression of mitochondrial calcium uniporter (MCU). Results are shown as nmoles oxidized cytochrome c/min/mg of mitochondrial protein.

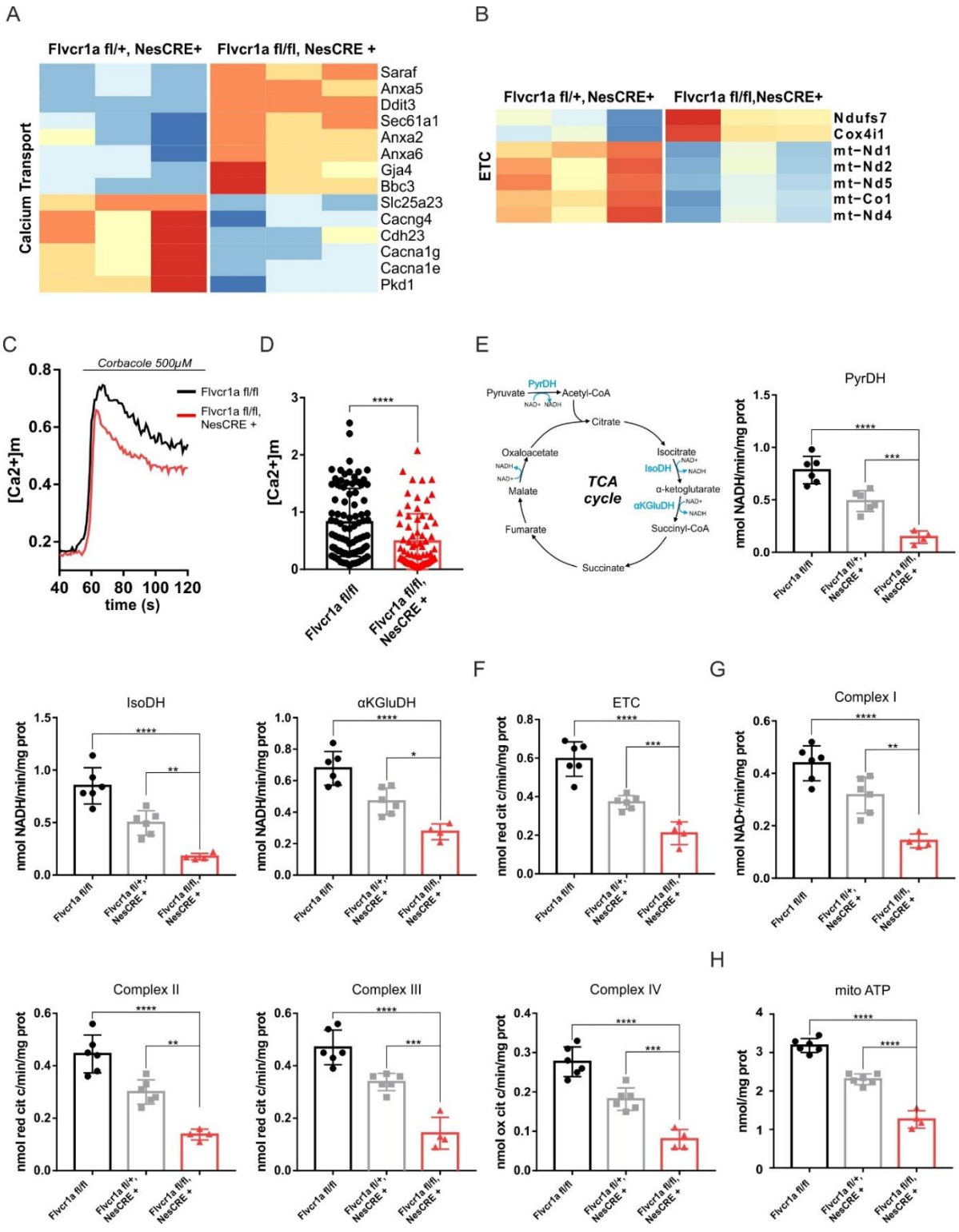
A
Flvcr1a fl/+, NesCRE+
Flvcr1a fl/fl, NesCRE +
Calcium Transport
Saraf
Anxa5
Ddit3
Sec61a1
Anxa2
Anxa6
Gja4
Bbc3
Slc25a23
Cacng4
Cdh23
Cacna1g
Cacna1e
Pkd1
B
Flvcr1a fl/+, NesCRE+
Flvcr1a fl/fl,NesCRE+
ETC
Ndufs7
Cox4i1
mt-Nd1
mt-Nd2
mt-Nd5
mt-Co1
mt-Nd4
C
Corbacole 500μM
Flvcr1a fl/fl
Flvcr1a fl/fl, NesCRE +
[Ca2+]m
time (s)
D
[Ca2+]m
Flvcr1a fl/fl
Flvcr1a fl/fl, NesCRE +
E
PyrDH
Pyruvate
Acetyl-CoA
Citrate
Isocitrate
IsoDH
α-ketoglutarate
αKGluDH
Succinyl-CoA
Succinate
Fumarate
Malate
Oxaloacetate
TCA cycle
PyrDH
nmol NADH/min/mg prot
F
IsoDH
αKGluDH
ETC
nmol red cit c/min/mg prot
G
Complex I
nmol NAD+/min/mg prot
H
Complex II
Complex III
Complex IV
nmol ox cit c/min/mg prot
mito ATP
nmol/mg prot

Figure 8. Loss of *Flvcr1a* in NSCs results in altered MAMs morphology and reduced calcium uptake in mitochondria, leading to metabolic impairments. (A) RNA-seq data showing altered expression of genes involved in calcium transport and homeostasis in *Flvcr1a*$^{fl/fl}$;NesCRE+ mutant compared to *Flvcr1a*$^{fl/+}$;NesCRE+ brains. **(B)** Heat map showing altered expression of genes encoding the electron transport chain (ETC) complexes in E14.5 *Flvcr1a*$^{fl/fl}$;NesCRE+ brains. **(C)** Mitochondrial calcium uptake measured as calcium (Ca2+) responses to agonist stimulation (500 µM carbachol) in mouse primary neural progenitor cells (NSCs) isolated from *Flvcr1a*$^{fl/fl}$;NesCRE+ mutant and *Flvcr1a*$^{fl/+}$;NesCRE+ brains. The fluorescent probe mito-GEM-GECO1 was used. Representative Ca2+ traces are shown. **(D)** Quantification of peak mitochondrial calcium amplitude in NPC upon agonist stimulation, from three independent experiments. (T-test; **=P<0.01.) **(E)** Activity of the Pyruvate, Isocitrate and αketoglutarate dehydrogenases, the key enzymes of the TCA cycle regulated by calcium, in NSCs isolated from *Flvcr1a*$^{fl/fl}$;NesCRE+ mutant and *Flvcr1a*$^{fl/+}$;NesCRE+ and *Flvcr1a*$^{fl/fl}$ control brains. Results are expressed as nmoles NADH/min/mg of mitochondrial protein. **(F)** Activity of the mitochondrial electron transport chain (ETC) complexes I-III in NSCs isolated from *Flvcr1a*$^{fl/fl}$;NesCRE+ mutant and *Flvcr1a*$^{fl/+}$;NesCRE+ and *Flvcr1a*$^{fl/fl}$ control brains. Results are shown as nmoles reduced cytochrome c/min/mg of mitochondrial protein. **(G)** Activity of the mitochondrial electron transport chain (ETC) complexes I,II,III and IV in NSCs isolated from *Flvcr1a*$^{fl/fl}$;NesCRE+ mutant and *Flvcr1a*$^{fl/+}$;NesCRE+ and *Flvcr1a*$^{fl/fl}$ control brains. Results are shown as nmoles of NAD+/min/mg of mitochondrial protein for complex I, nmoles reduced cytochrome c/min/mg of mitochondrial protein for complex II and III, nmoles oxidized cytochrome c/min/mg of mitochondrial protein. **(H)** Mitochondrial ATP levels as measured by a bioluminescence assay from NSCs isolated from *Flvcr1a*$^{fl/fl}$;NesCRE+ mutant and *Flvcr1a*$^{fl/+}$;NesCRE+ and *Flvcr1a*$^{fl/fl}$ control brains. Results are shown as nmoles ATP/mg of mitochondrial proteins. (One-Way ANOVA; *=P<0.05; **=P<0.01; ***=P<0.001; ****=P<0.0001.)

Supplementary Figures

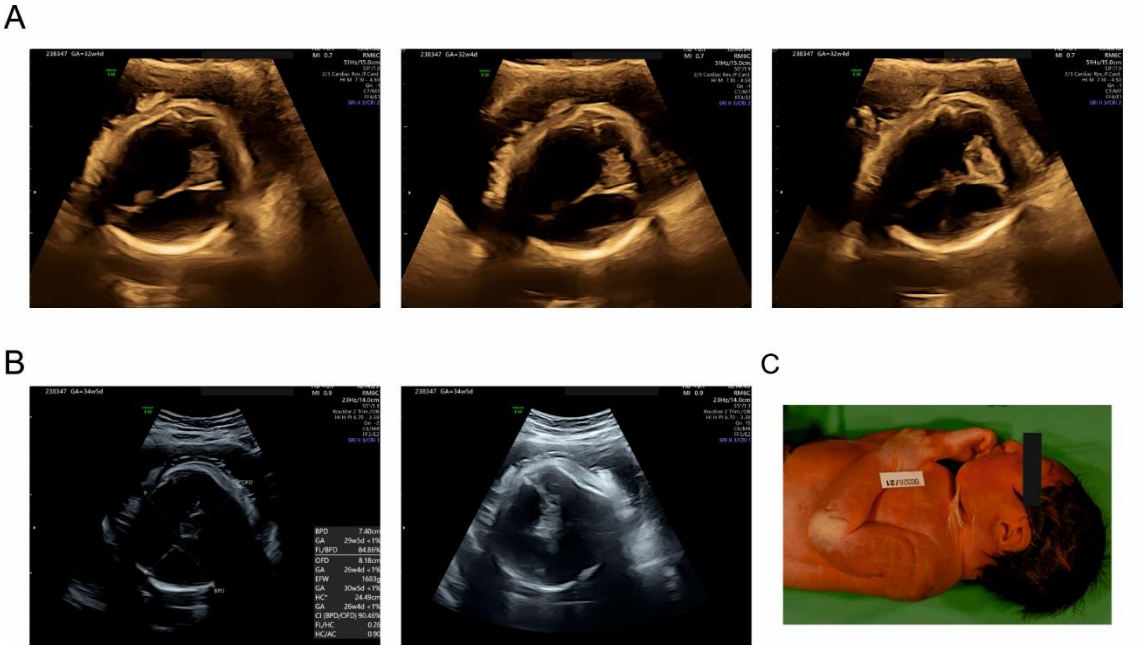

Figure S1. Macroscopic and Sonographic evaluation of the male fetus carrying a homozygous inactivating mutation in the *FLVCR1* gene.

(A) Sonographic examinations of 32 + 4 weeks of pregnancy. **(B)** Sonographic examinations of 34 + 5 weeks of pregnancy. Sonographic examinations show extreme microcephaly with anechoic skull and no evidence of cerebral tissue. **(C)** Macroscopic evaluation showed an immature male fetus of the 35th gestational week with microcephaly and hydrocephalus with only rudimentary cerebral structures and no indication of visceral anomalies.

A

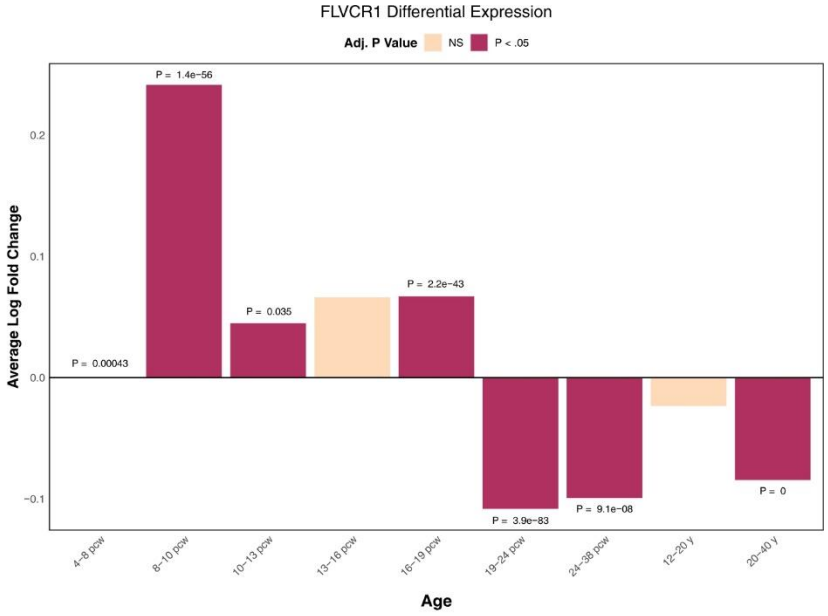
FLVCR1 Differential Expression
Adj. P Value
NS
P < .05
Average Log Fold Change
0.2
0.1
0.0
−0.1
P = 0.00043
P = 1.4e−56
P = 0.035
P = 2.2e−43
P = 3.9e−83
P = 9.1e−08
P = 0
4−8 pcw
8−10 pcw
10−13 pcw
13−16 pcw
16−19 pcw
19−24 pcw
24−38 pcw
12−20 y
20−40 y
Age

B

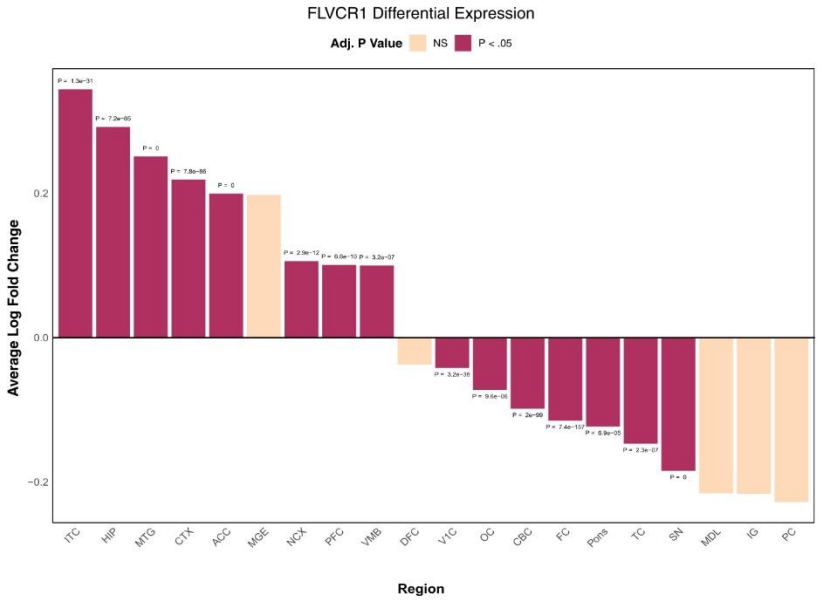
FLVCR1 Differential Expression
Adj. P Value
NS
P < .05
Average Log Fold Change
0.2
0.0
−0.2
ITC
HIP
MTG
CTX
ACC
MGE
NCX
PFC
VMB
DFC
V1C
OC
CBC
FC
Pons
TC
SN
MDL
IG
PC
Region

C

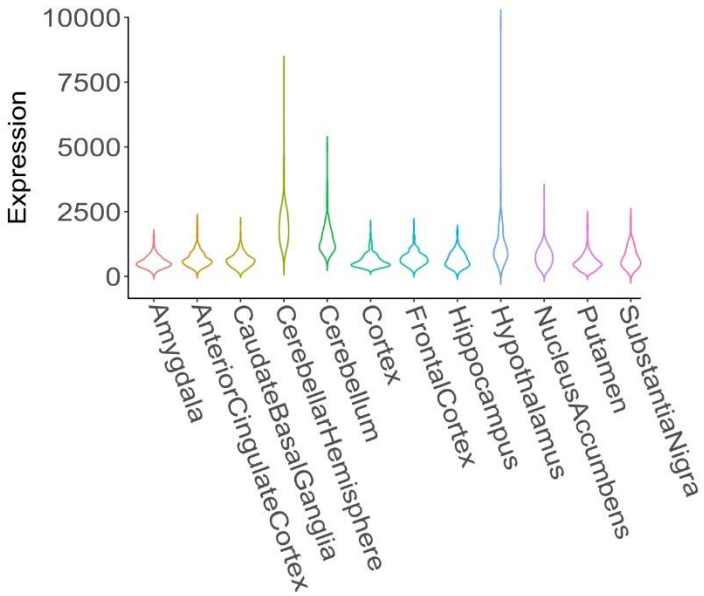
Expression
10000
7500
5000
2500
0
Amygdala
AnteriorCingulateCortex
CaudateBasalGanglia
CerebellarHemisphere
Cerebellum
Cortex
FrontalCortex
Hippocampus
Hypothalamus
NucleusAccumbens
Putamen
SubstantiaNigra

Figure S2. FLVCR1a expression pattern in developmental and adult human brain

(A) Differential expression of FLVCR1 across developmental periods in a single-cell data set of over 100,000 cells. PCW, postconceptional weeks; Y, years; **(B)** Differential expression of FLVCR1 across different brain regions in a single-cell data set of over 100,000 cells spanning from 4 PCW to 40 years old. **(C)** Allen Brain Atlas analysis of FLVCR1a expression in the adult human brain.

ACC, anterior cingulate cortex; CBC, cerebellar cortex; CTX, cortex; DFC, dorsolateral prefrontal cortex; FC, frontal cortex; HIP, hippocampus; IG, insular gyris; ITC, inferior temporal cortex; MDL, medulla; MGE, medial ganglionic eminence; MTG, middle temporal gyrus; NCX, neocortex; OC, occipital cortex; PC, parietal cortex; PFC, prefrontal cortex; SN, substantia nigra; TC, temporal cortex; V1C, primary visual cortex; VMB, ventral midbrain; PCW, postconceptional weeks; Y, years;

A

B

	FL/+	FL/FL	FL/+; CRE+	FL/FL; CRE+	
	n	n	n	n	N
E14,5	6 (17%)	9 (26%)	12 (34%)	8 (23%)	35
E18,5	10 (25%)	12 (28%)	8 (20%)	10 (25%)	40
P0	3 (13%)	4 (17%)	10 (43%)	5 (22%)	23
P21	23 (48%)	12 (25%)	13(27%)	0	48

C

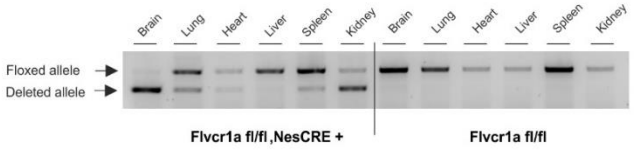

D

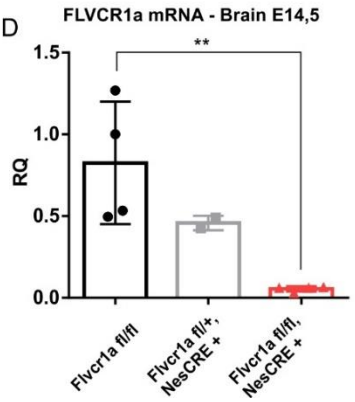

Figure S3. Generation of conditional knockout mice lacking Flvcr1a exclusively in neuronal progenitors (Flvcr1a fl/fl;NesCRE+).

(A) Newborns derived from crossing Flvcr1a fl/+; NesCRE+ and Flvcr1a fl/fl mice. A representative picture is shown. **(B)** Genotyping of embryos and pups derived by crossing Flvcr1a fl/+;NesCRE+ and Flvcr1a fl/fl mice. **(C)** The deletion of Flvcr1a was confirmed by PCR on genomic DNA from P0 Flvcr1a fl/fl;NesCRE+ and Flvcr1a fl/fl embryos. The floxed and deleted alleles were amplified using the primers indicated in the methods section. A representative picture is shown. **(D)** qRT-PCR analysis of Flvcr1a mRNA in E14.5 brains dissected from Flvcr1a fl/fl;NesCRE+ and Flvcr1a fl/fl embryos. One Way ANOVA. **=P<0.01.

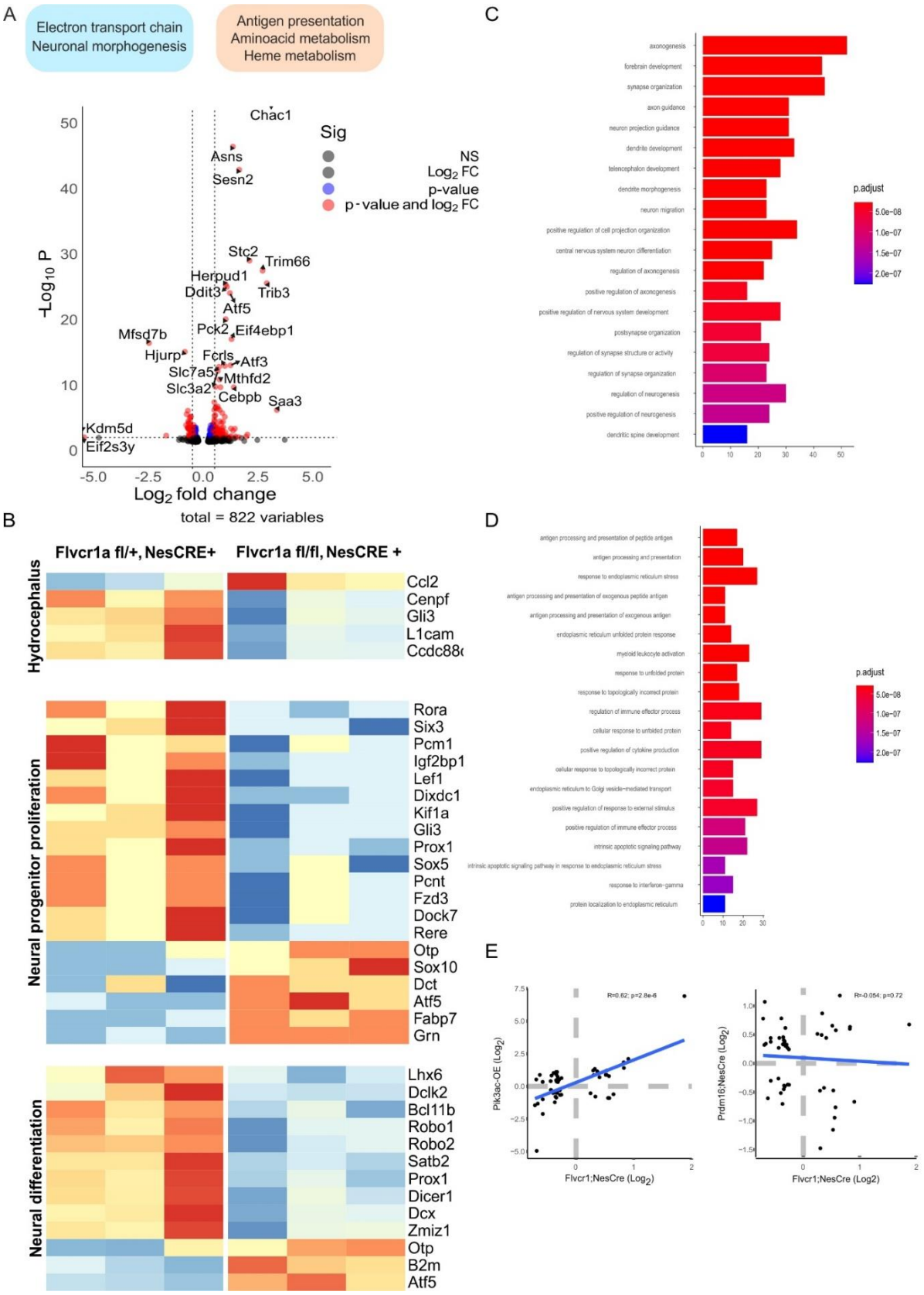
A
Electron transport chain
Neuronal morphogenesis
Antigen presentation
Aminoacid metabolism
Heme metabolism
Sig
NS
Log2 FC
p-value
p-value and log2 FC
-Log10 P
Log2 fold change
total = 822 variables
Chac1
Asns
Sesn2
Stc2
Trim66
Herpud1
Ddit3
Trib3
Atf5
Pck2
Eif4ebp1
Mfsd7b
Hjurp
Fcrls
Atf3
Slc7a5
Mthfd2
Slc3a2
Cebpb
Saa3
Kdm5d
Eif2s3y
B
Flvcr1a fl/+, NesCRE+
Flvcr1a fl/fl, NesCRE +
Hydrocephalus
Ccl2
Cenpf
Gli3
L1cam
Neural progenitor proliferation
Rora
Six3
Pcm1
Igf2bp1
Lef1
Dixdc1
Kif1a
Gli3
Prox1
Sox5
Pcnt
Fzd3
Dock7
Rere
Otp
Sox10
Dct
Atf5
Fabp7
Grn
Neural differentiation
Lhx6
Dclk2
Bcl11b
Robo1
Robo2
Satb2
Prox1
Dicer1
Dcx
Zmiz1
Otp
B2m
Atf5
C
axonogenesis
forebrain development
synapse organization
axon guidance
neuron projection guidance
dendrite development
telencephalon development
dendrite morphogenesis
neuron migration
positive regulation of cell projection organization
central nervous system neuron differentiation
regulation of axonogenesis
positive regulation of axonogenesis
positive regulation of nervous system development
postsynapse organization
regulation of synapse structure or activity
regulation of synapse organization
regulation of neurogenesis
positive regulation of neurogenesis
dendritic spine development
p.adjust
D
antigen processing and presentation of peptide antigen
antigen processing and presentation
response to endoplasmic reticulum stress
antigen processing and presentation of exogenous peptide antigen
antigen processing and presentation of exogenous antigen
endoplasmic reticulum unfolded protein response
myeloid leukocyte activation
response to unfolded protein
response to topologically incorrect protein
regulation of immune effector process
cellular response to unfolded protein
positive regulation of cytokine production
cellular response to topologically incorrect protein
endoplasmic reticulum to Golgi vesicle-mediated transport
positive regulation of response to external stimulus
positive regulation of immune effector process
intrinsic apoptotic signaling pathway
intrinsic apoptotic signaling pathway in response to endoplasmic reticulum stress
response to interferon-gamma
protein localization to endoplasmic reticulum
p.adjust
E
R=0.82; p=2.8e-8
Pik3ac-OE (Log2)
Flvcr1;NesCre (Log2)
R=-0.054; p=0.72
Prdm16;NesCre (Log2)
Flvcr1;NesCre (Log2)

Figure S4. RNA-seq analysis of E14.5 Flvcr1a fl/fl;NesCRE+ brains highlighted impaired neurogenesis

(A) Volcano plot of most downregulated and upregulated terms in the E14.5 Flvcr1a fl/fl;NesCRE+ brain highlights electron transport chain among the most downregulated terms and heme metabolism among the most upregulated. **(B)** Heat map showing altered expression of genes involved in hydrocephalus, neural progenitor proliferation and differentiation in E14.5 Flvcr1a fl/fl;NesCRE+ brains compared to E14.5 Flvcr1a fl/+;NesCRE+ control brains **(C)** Gene ontology analysis of biological processes in Flvcr1a fl/fl;NesCRE+ E14.5 brains. **(D)** Gene ontology analysis of biological processes in Flvcr1a fl/fl;NesCRE+ E14.5 brains. **(E)** Linear regression plots of genes differentially expressed in Flvcr1a and Pik3ac-OE model and in Flvcr1a and Prdm16 OE model.

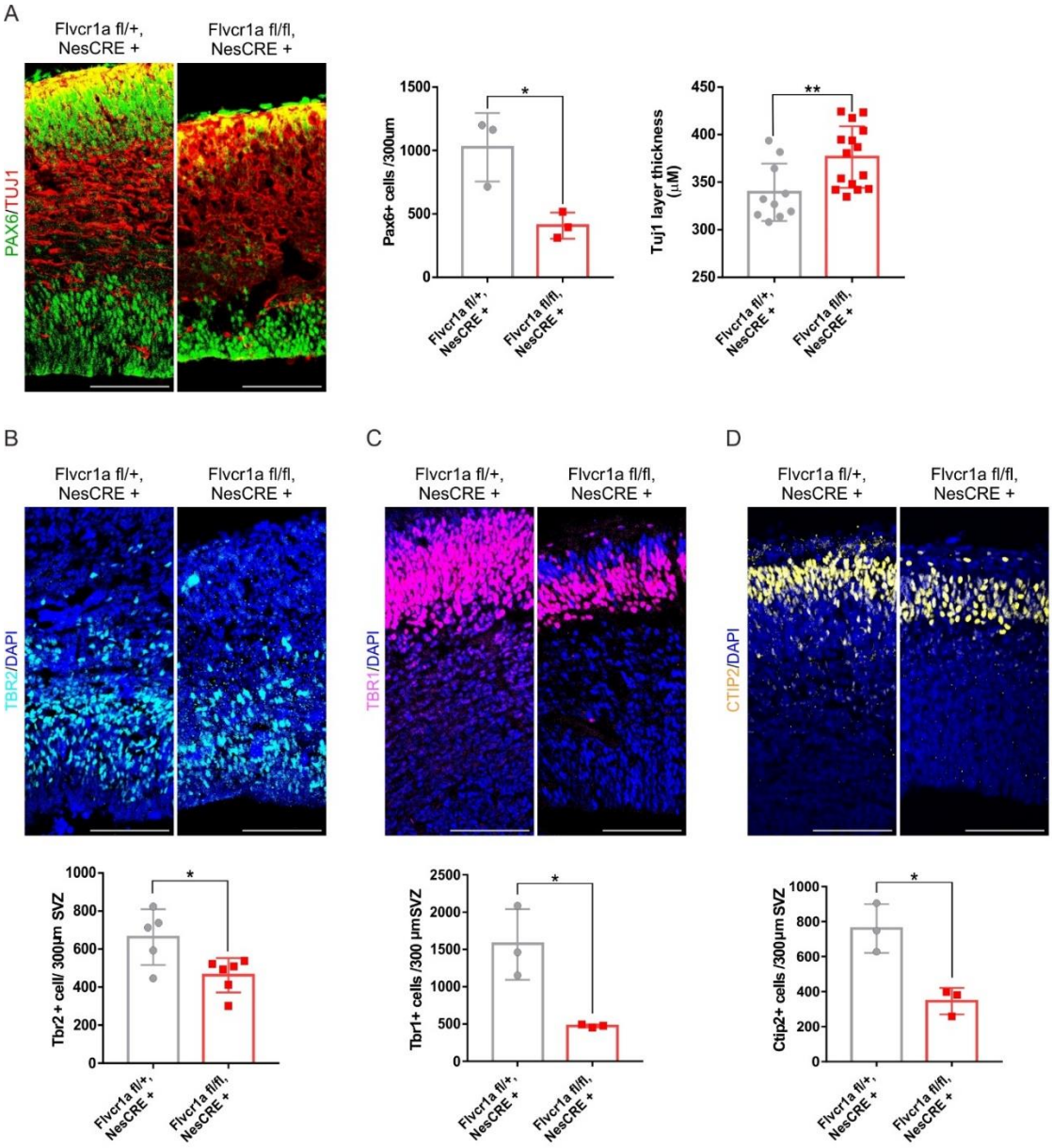

Figure S5. Flvcr1a loss in mouse neuronal progenitors results in reduced cortex thickness and reduced number of radial glia (RGCs), intermediate progenitors (IPs) and cortical neurons at E16.5. (A) Immunostaining of PAX6 (RGCs) and TUJ1 (cortical neurons) in Flvcr1a fl/fl;NesCRE+ and Flvcr1a fl/+;NesCRE+ control mouse cortex. Each dot represents the mean of 3 images quantified from each animal. n=3. Scale bar=100µm. **(B)** Immunostaining of TBR2 (IPs) in Flvcr1a fl/fl;NesCRE+ and Flvcr1a fl/+;NesCRE+ control mouse cortex. Each dot corresponds to the mean of three different measurements. Scale bar=100µm. **(C)** Immunostaining of TBR1 (cortical neurons) in Flvcr1a fl/fl;NesCRE+ and Flvcr1a fl/+;NesCRE+ control mouse cortex. Each dot corresponds to the mean of three different measurements. Scale bar=100µm. **(D)** Immunostaining of CTIP2 (cortical neurons) in Flvcr1a fl/fl;NesCRE+ and Flvcr1a fl/+;NesCRE+

control mouse cortex. Each dot corresponds to the mean of three different measurements. Scale bar=100µm. T-Test. *=P<0.05; **=P<0.01.

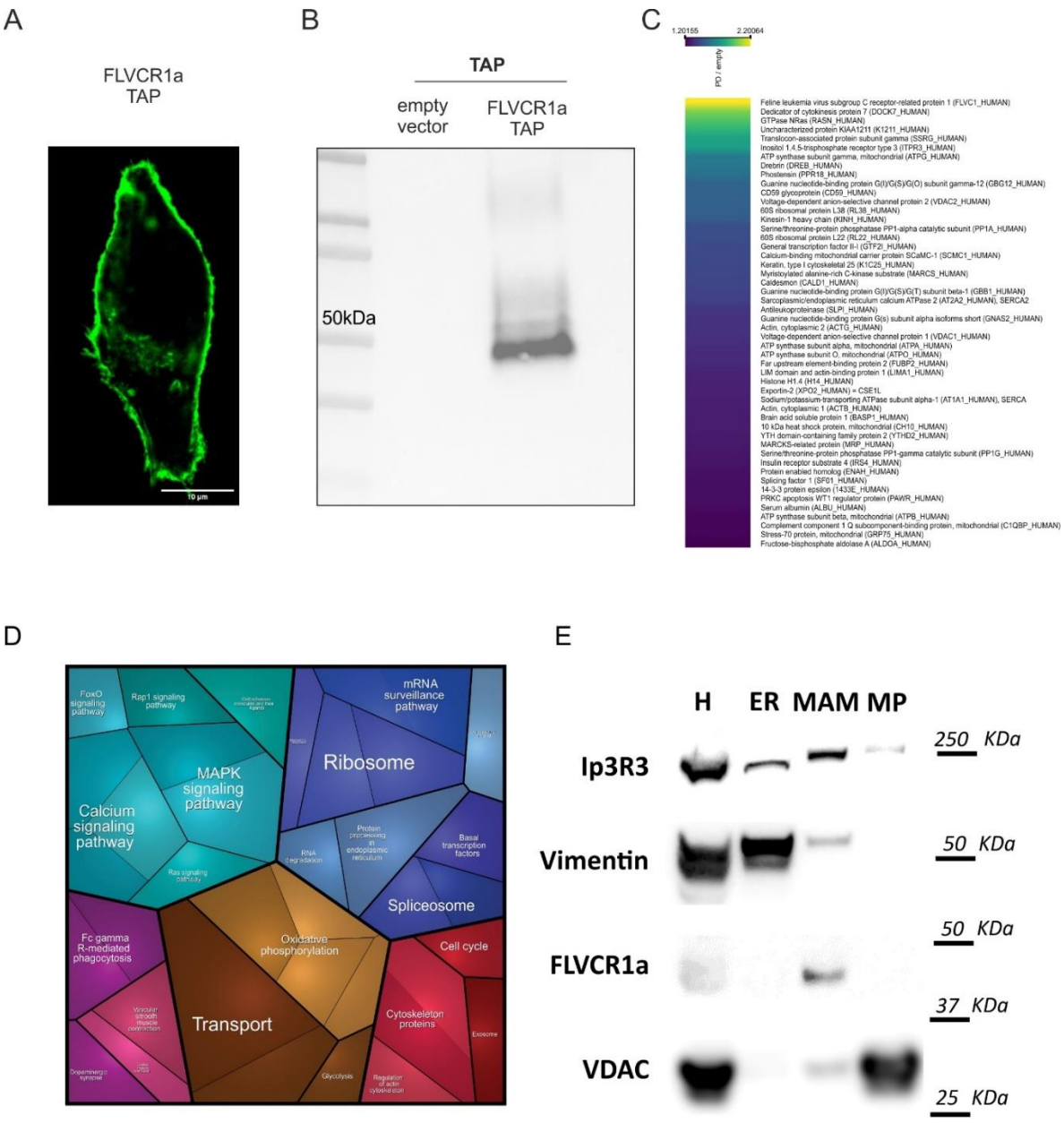

Figure S6. FLVCR1a interactome revealed an undescribed localization at MAMs.

(A) Immunofluorescence analysis of HeLa cells transiently overexpressing FLVCR1a-TAP. Scale bar=10µm. **(B)** Western Blot of FLVCR1a following TAP purification. An antibody against FLVCR1a was used. **(C)** Top 50 FLVCR1a interactors, stratified based on the ratio of FLVCR1a-TAP pulldown/empty and sorted for highest enriched proteins from top to lowest on the bottom. **(D)** Proteomaps Voronoi plot based on the top 50 enriched proteins after the pulldown. **(E)** Subcellular fractioning of HeLa cells demonstrates FLVCR1a localization at MAMs. H=homogenate; ER=endoplasmic reticulum; MAM= mitochondria associated membranes PM=pure mitochondria

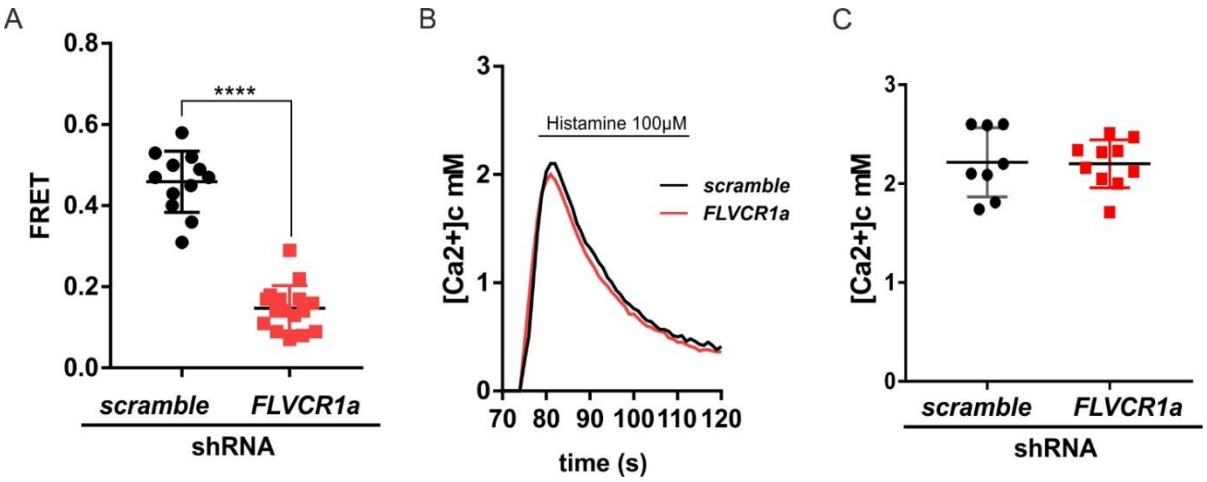

Figure S7. Cytosolic and mitochondrial calcium elevation following agonist stimulation in FLVCR1a-down modulated and control HeLa cells.

(A) Mitochondrial calcium elevation following agonist stimulation (Histamine) in HeLa cells using a FRET-based probe. The calcium increase is calculated based on FRET efficiency **(B)** Representative kinetics of the cytosolic calcium elevation upon Histamine stimulation in FLVCR1a-downmodulated and control HeLa cells using the cytosolic aequorin probe. **(C)** Quantification of peak cytosolic calcium amplitude from two independent experiments. T-test. ****=P<0.0001.

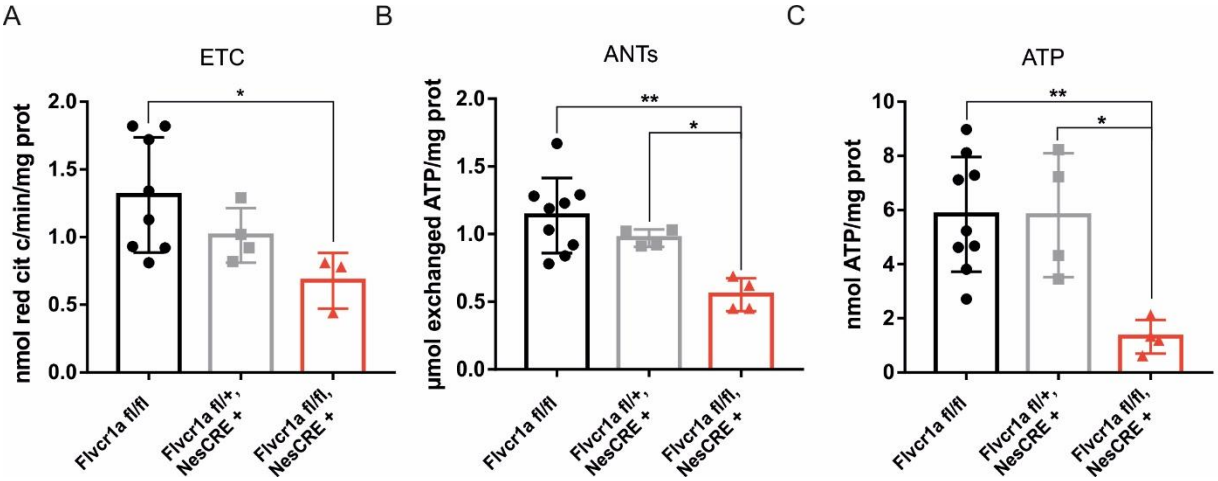

Figure S8. Reduced oxidative metabolism in E14.5 Flvcr1a fl/fl;NesCRE+ total brains. (A) Activity of the mitochondrial electron transport chain (ETC) complexes I-III in Flvcr1a fl/fl;NesCRE+ mutant and Flvcr1a fl/fl, Flvcr1a fl/+;NesCRE+ control brains. Results are shown as nmoles reduced cytochrome c/ min/mg of mitochondrial protein. **(B)** Mitochondria ANTs activity in Flvcr1a fl/fl;NesCRE+ mutant and Flvcr1a fl/fl, Flvcr1a fl/+;NesCRE+ control brains. Results are expressed as µmoles exchanged ATP/mg mitochondrial protein. **(C)** ATP levels measured by a bioluminescence assay. Results are shown as nmoles ATP/mg of mitochondrial proteins. T-test. *=P<0.05; **=P<0.01.

Acknowledgments

Volevo ringraziare Emanuela e Deborah, le mie due supervisors, per avermi permesso di svolgere il mio PhD nel loro laboratorio, per avermi formato in questi anni e permesso di viaggiare e imparare anche in altri laboratori.

Volevo ringraziare anche tutti i membri del laboratorio Tolosano/Altruda/Chiabrando. Dai post-doc, ai dottorandi a tutti gli studenti che hanno trascorso da qualche settimana a interi anni qui con me in laboratorio. Porterò con me ogni riunione, congresso e ogni momento più leggero trascorso insieme.

Un grazie quasi infinito va e andrà sempre ai miei genitori. Grazie per essere qui oggi con me, grazie per esserci sempre e per sostenermi sempre e comunque, qualsiasi imprevisto la vita mi proporrà so che voi sarete lì ad aiutarmi.

Grazie a mia sorella Federica, grazie per essere così uguale e così diversa. Grazie perché quasi non riesco ad esprimere a parole quanto mi hai aiutata, soprattutto ultimamente. Sei il mio cuore.

Grazie ad Andrea, grazie per il sostegno che mi dai e per avermi fatto capire la bellezza della semplicità e della quotidianità insieme.

Grazie a mia nonna, ai miei zii e a mia cugina, siamo una piccola famiglia ma da sempre ho colto l'amore che ci unisce.

Grazie a Sara, Diana e Flaminia, i miei cuori da sempre.

Grazie ad Anna e Giorgia, grazie per avermi aiutata sempre, in laboratorio e fuori. Sono sicura che tutto il mio percorso sarebbe stato diverso senza di voi.

Grazie alle mie amiche di sempre, ai miei amici più recenti e ai miei amici lontani. Grazie a tutti i miei colleghi per essere diventati amici. Siete tanti e tutti preziosi per me. Grazie per aver condiviso questo percorso insieme.

Un’estremamente grata e felice Franci.